

Remote Sensing of Surface Melt on Antarctica Opportunities and Challenges

de Roda Husman, Sophie; Hu, Zhongyang; Wouters, Bert; Munneke, Peter Kuipers; Veldhuijsen, Sanne; Lhermitte, Stef

DOI

[10.1109/JSTARS.2022.3216953](https://doi.org/10.1109/JSTARS.2022.3216953)

Publication date

2022

Document Version

Final published version

Published in

IEEE Journal of Selected Topics in Applied Earth Observations and Remote Sensing

Citation (APA)

de Roda Husman, S., Hu, Z., Wouters, B., Munneke, P. K., Veldhuijsen, S., & Lhermitte, S. (2022). Remote Sensing of Surface Melt on Antarctica: Opportunities and Challenges. *IEEE Journal of Selected Topics in Applied Earth Observations and Remote Sensing*, 16, 2462-2480.
<https://doi.org/10.1109/JSTARS.2022.3216953>

Important note

To cite this publication, please use the final published version (if applicable).
Please check the document version above.


Copyright

Other than for strictly personal use, it is not permitted to download, forward or distribute the text or part of it, without the consent of the author(s) and/or copyright holder(s), unless the work is under an open content license such as Creative Commons.

Takedown policy

Please contact us and provide details if you believe this document breaches copyrights.
We will remove access to the work immediately and investigate your claim.

Remote Sensing of Surface Melt on Antarctica: Opportunities and Challenges

Sophie de Roda Husman , Zhongyang Hu , Bert Wouters , Peter Kuipers Munneke , Sanne Veldhuijsen ,
and Stef Lhermitte 

Abstract—Surface melt is an important driver of ice shelf disintegration and its consequent mass loss over the Antarctic Ice Sheet. Monitoring surface melt using satellite remote sensing can enhance our understanding of ice shelf stability. However, the sensors do not measure the actual physical process of surface melt, but rather observe the presence of liquid water. Moreover, the sensor observations are influenced by the sensor characteristics and surface properties. Therefore, large inconsistencies can exist in the derived melt estimates from different sensors. In this study, we apply state-of-the-art melt detection algorithms to four frequently used remote sensing sensors, i.e., two active microwave sensors, which are Advanced Scatterometer (ASCAT) and Sentinel-1, a passive microwave sensor, i.e., Special Sensor Microwave Imager/Sounder (SSMIS), and an optical sensor, i.e., Moderate Resolution Imaging Spectroradiometer (MODIS). We intercompare the melt detection results over the entire Antarctic Ice Sheet and four selected study regions for the melt seasons 2015–2020. Our results show large spatiotemporal differences in detected melt between the sensors, with particular disagreement in blue ice areas, in aquifer regions, and during wintertime surface melt. We discuss that discrepancies between sensors are mainly due to cloud obstruction and polar darkness, frequency-dependent penetration of satellite signals, temporal resolution, and spatial resolution, as well as the applied melt detection methods. Nevertheless, we argue that different sensors can complement each other, enabling improved detection of surface melt over the Antarctic Ice Sheet.

Index Terms—Antarctic Ice Sheet, Earth observation, ice shelves, melt detection, multisource remote sensing, polar regions, satellite observations.

Manuscript received 31 May 2022; revised 17 September 2022; accepted 14 October 2022. Date of publication 25 October 2022; date of current version 10 March 2023. The work of Sophie de Roda Husman and Sanne Veldhuijsen was supported by Nederlandse Organisatie voor Wetenschappelijk Onderzoek (NWO) under Grant OCENW.GROOT.2019.091. The work of Zhongyang Hu was supported by the Netherlands Space Office (NSO) under Grant ALWGO.2018.039. (Sophie de Roda Husman and Zhongyang Hu contributed equally to this work.) (Corresponding author: Sophie de Roda Husman.)

Sophie de Roda Husman is with the Department of Geoscience and Remote Sensing, Delft University of Technology, 2628 CD Delft, The Netherlands (e-mail: s.derodahusman@tudelft.nl).

Bert Wouters is with the Department of Geoscience and Remote Sensing, Delft University of Technology, 2628 CD Delft, The Netherlands, and also with the Institute for Marine and Atmospheric Research Utrecht, Utrecht University, 3584 CS Utrecht, The Netherlands (e-mail: bert.wouters@tudelft.nl).

Zhongyang Hu, Peter Kuipers Munneke, and Sanne Veldhuijsen are with the Institute for Marine and Atmospheric Research Utrecht, Utrecht University, 3584 CS Utrecht, The Netherlands (e-mail: z.hu@uu.nl; p.kuipersmunneke@uu.nl; s.b.m.veldhuijsen@uu.nl).

Stef Lhermitte is with the Department of Geoscience and Remote Sensing, Delft University of Technology, 2628 CD Delft, The Netherlands, and also with the Department of Earth and Environmental Sciences, KU Leuven, 3000 Leuven, Belgium (e-mail: s.lhermitte@tudelft.nl).

Digital Object Identifier 10.1109/JSTARS.2022.3216953

I. INTRODUCTION

LARGE uncertainty about the future viability of the Antarctic ice shelves leads to an enormous spread in sea level rise projections [1], [2], [3], [4], [5]. Estimates on the contribution of the Antarctic Ice Sheet over the next century range from +0.03 to +0.34 m of sea level equivalent under Representative Concentration Pathway 8.5 according to the Sixth Assessment Report [4]. By far the largest direct contribution to the present day Antarctic Ice Sheet mass loss is enhanced basal melt and increased iceberg calving. In the mass balance of Antarctica, direct mass loss by surface melt and subsequent runoff currently play a marginal role [6], [7]. However, surface melt can lead to enhanced mass loss indirectly, by destabilization of ice shelves [8], [9], [10], [11]. When melt ponds drain into crevasses in the ice shelf, the stress of the meltwater column exerted on the crevasse tip can promote fracture, resulting in a weakened ice shelf [12], [13]. Moreover, the load of meltwater lakes causes flexural stresses in the ice shelf that generate fractures, further weakening the ice shelf [14], [15], [16]. Recent climate models that incorporate the impact of meltwater on ice shelf instability (e.g., [17]) suggest that surface meltwater will result in widespread melting and hydrofracturing during this century, leading to a significant increase in the contribution of the Antarctic Ice Sheet to sea level rise. Regardless of the ice shelf processes in these models, Antarctic surface melt is projected to double by 2050 due to atmospheric warming [10], [18]. In this context, monitoring the presence of surface melt on the Antarctic ice shelves can improve our understanding of the fundamental processes involved in the coupling between meltwater production and future Antarctic mass loss, ultimately improving our sea level rise projections and reducing their uncertainties.

At present, there are three methods to estimate surface melt, using: 1) automatic weather stations (AWSs); 2) physics-based (regional) climate models (RCMs); and 3) remote sensing. First, AWS observations can be used to compute the surface energy balance and estimate the excess energy available for surface melt. For instance, Vaughan [19] studied observations from nine AWSs dating back to 1947, solely using temperature data. Studies followed that used more sophisticated AWSs equipped with radiation sensors [9], [20]. While AWS observations are widely used and considered “ground truth” [21], the main drawback of AWS observations is that the data are point-based on a limited number of locations, making them insufficient for continent-wide melt studies. Moreover, AWS locations are heavily biased toward homogeneous snow surface types, disregarding more

challenging surface types, such as blue ice, slush, and other wet surface types.

The second approach to estimate surface melt is using RCMs, such as *Modèle Atmosphérique Régional* (e.g., [22]) or *Regional Atmospheric Climate Model (RACMO2)* (e.g., [23]). RCMs can simulate surface melt on a continental scale. Nevertheless, the accuracy of models relies on the resolution and accuracy of its forcing data, which are often unsatisfactory for the Antarctic Ice Sheet [24]. Moreover, melt features over low albedo regions are often more detailed than the model resolution and can therefore not accurately be captured by RCMs [25], [26], [27].

Remote sensing is an alternative to derive long-term (back to 1970s) melt dynamics at various spatiotemporal resolutions. Optical sensors have been used not only to detect meltwater presence, such as supraglacial streams, lakes [26], [28], [29], and slush [30], but also to estimate meltwater extent [25], [31], [32], [33] and volume [34], [35], [36]. Microwave sensors have also been used for detecting the presence of meltwater, for example, the active microwave Ku-band (12–18 GHz) from *Quick Scatterometer (QuikSCAT)* [37], C-band (4–8 GHz) from *Advanced Scatterometer (ASCAT)* [38] and *Sentinel-1* [39], [40], [41], [42], [43], and passive microwave K-band (18–27 GHz) and K_a -band (27–40 GHz) from *Scanning Multichannel Microwave Radiometer (SSMR)* and *Special Sensor Microwave/Imagers (SSM/I)* [44], [45], [46], [47], [48], and L-band (1–2 GHz) sensors, such as *Soil Moisture Active Passive (SMAP)* [49], [50] and *Soil Moisture and Ocean Salinity (SMOS)* [51]. Attempts to convert binary detected surface melt to continuous estimates of meltwater volume have been carried out using *QuikSCAT* [52] and *Special Sensor Microwave Imager/Sounder (SSMIS)* (over Greenland, [53]).

Remote sensing satellites provide information on the Antarctic surface in the visible to the microwave part of the electromagnetic spectrum, i.e., surface reflectance, backscatter intensity (σ^0), and brightness temperature (T_b). The values of surface reflectance, σ^0 , and T_b are altered under the presence of liquid water. These parameters therefore are indicators for the presence of liquid water, rather than for the actual physical process of surface melt, which is in fact an energy (conversion) process, except, perhaps, in the case of thermal-infrared-derived surface temperature that defines the occurrence of surface melt at the melting point. Yet, the term “surface melt” is widely used in the remote sensing community (e.g., [10], [16], [18], [20]), and we will adopt it here, although we do acknowledge that sensors measure the presence of liquid water. Apart from this, spaceborne observations of backscatter intensity, brightness temperature, and surface reflectance depend on sensor characteristics and surface properties. In this regard, large inconsistencies can exist in derived surface melt estimates from different sensors [24].

This study aims to identify the opportunities and challenges for melt detection over the Antarctic Ice Sheet using remote sensing, focusing on currently operating sensors that are capable of detecting wet surfaces (e.g., wet snow, slush, melt ponds, and streams). We compare differences in melt detection among a frequently used radiometer (i.e., SSMIS), scatterometer (i.e., ASCAT), synthetic aperture radar sensor (i.e., Sentinel-1), and optical sensor [i.e., *Moderate Resolution Imaging Spectroradiometer (MODIS)*]. In this study, we exclude sensors that are

no longer operational (such as QuikSCAT). Moreover, L-band sensors (such as SMOS and SMAP) are not considered, as they are less sensitive to surface melt than K-band and K_a -band sensors (such as SSMIS) [51].

The rest of this article is organized as follows. In Section II, we introduce the background of monitoring surface melt using different sensors and related research. In Section III, we introduce the satellite and auxiliary datasets. Then, we summarize the state-of-the-art methods we applied for surface melt detection in Section IV separately for each sensor type. In Section V, we apply the melt detection methods to MODIS, Sentinel-1, ASCAT, and SSMIS over the entire Antarctic Ice Sheet for melt seasons 2015–2020. We compare spatial and temporal patterns of retrieved surface melt and assess the sensitivity of the methods. Based on this intercomparison, we discuss the possibilities and challenges of the different sensors and methods in Section VI. Finally, Section VII concludes this article.

II. BACKGROUND AND RELATED RESEARCH

Before applying melt detection algorithms to the sensor observations, we illustrate *what* satellite sensors are detecting and *how* this is linked to surface melt. Fig. 1 shows the measuring principles of optical, active microwave, and passive microwave sensors under different atmospheric and melting conditions. In this study, we focus on active microwave sensors (i.e., ASCAT and Sentinel-1) that operate at frequencies between 5.2 and 5.4 GHz (C-band; wavelength of 5.6 cm), and passive microwave sensors at 19 GHz (K-band; wavelength: 1.6 cm) and at 37 GHz (K_a -band; wavelength of 0.8 cm). Fig. 1(a) shows a dry snowpack in which active microwave sensors can penetrate to a depth of around 10 m [54], passive microwave sensors to a smaller penetration depth of around 2.5 m for 19 GHz [and 0.5 m for 37 GHz, not shown in Fig. 1(a)] [54], whereas optical sensors only measure surface reflectance. Fig. 1(b) shows a snowpack under melting conditions under daylight and cloud-free conditions, and Fig. 1(c) shows the same melt situations, but in a cloudy and/or night situation. Signals from active and passive microwave sensors are (almost) unaffected by atmospheric conditions, whereas optical sensors depend on reflected sunlight. Fig. 1(d) shows near-surface melt presence, which can form due to near-surface melting [55], [56], after a snowfall event or after meltwater percolation from the surface [25].

Optical sensors measure the surface reflectance when atmospheric and topographical effects are removed from the visible through the shortwave infrared spectral bands. Since the total surface reflectance depends on the surface properties, the reflectance of snow, ice, water, and bare rocks can be used to discriminate between land surface types [57], [58], [59]. The refractive indices of water and ice are similar, and therefore do not directly change the surface reflectance when snow melts. However, the presence of liquid water changes the surface reflectance indirectly, because liquid water increases the snow grain size [59], [60]. Ponding water on the other hand changes the spectral properties of the surface, causing a drop in near-infrared, red, and green reflectance [61], [62]. This results in a blue appearance of melt components in true color imagery, such as slush, melt ponds, and streams [29], [30].

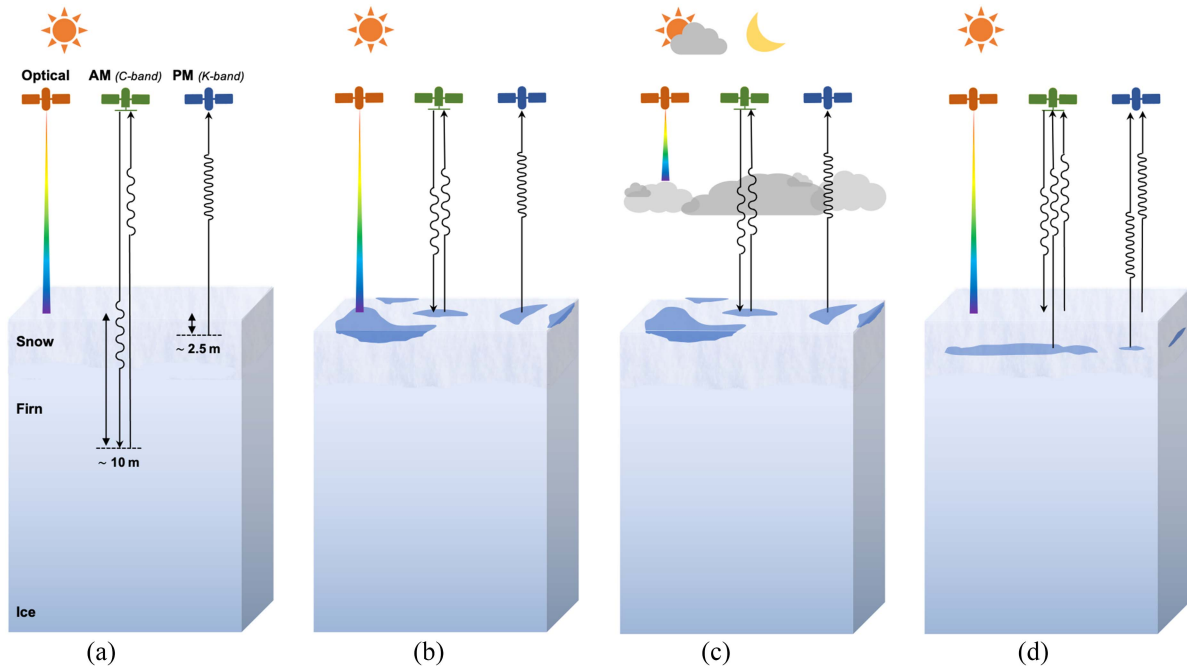


Fig. 1. Conceptual overview of working principles of optical, active, and passive microwave sensors under different atmospheric and melting conditions. (a) No melt and sunlight. (b) Surface melt and sunlight. (c) Surface melt and no sunlight due to cloudy and/or nighttime conditions. (d) Near-surface melt and sunlight. Here, AM indicates active microwave sensors and PM passive microwave sensors.

Active microwave sensors detect the reflected portion of a radar signal emitted by the satellite, known as the backscatter intensity. The backscatter intensity depends on the snow dielectric properties and the surface roughness, and hence is very sensitive to liquid water content within the snowpack [54]. Liquid water increases the absorption of the microwave radiation and also increases forward scattering, both leading to a decreased backscatter intensity compared to dry surfaces [48], [63]. Therefore, a drop in the backscatter intensity is associated with melt presence. Nevertheless, melt detection on surfaces with a very high or low roughness can be challenging. Surfaces may become rougher under the presence of liquid water, e.g., by creating small meltwater streams [64], [65]. This process increases the backscatter intensity, thereby confusing meltwater detection algorithms that look for a drop in backscatter intensity under melting conditions. Over very flat surfaces (e.g., blue ice), active microwave sensors might fail to detect surface melt, because sensors receive (almost) no backscattered signal during nonmelt periods [66], [67]. Hence, increased liquid water content does not further reduce the backscatter intensity.

Passive microwave sensors detect the brightness temperature, which is a function of the liquid water content, temperature, density, and grain size of the snowpack [68]. From all these factors, the liquid water content is assumed to have the largest influence on the brightness temperature [46], [69]. When snow melts, the liquid water content increases the imaginary part of the electromagnetic permittivity, which results in an increased brightness temperature [54], [70]. However, other factors, such as larger grain size, may also increase the brightness temperature, potentially leading to falsely detected melt.

Changes in remote sensing data form the basis for many melt detection algorithms. Most optical algorithms rely on thresholds based on a modified normalized difference water index adapted for ice ($NDWI_{ice}$) [34], [71], [72], [73], occasionally also including some additional thresholds [35]. Recently, machine learning techniques have been deployed for the detection of meltwater [29], [74] and slush [30]. However, it should be noted that besides the slush detection of Dell et al. [30], the listed methods focus on supraglacial lakes and streams, instead of the broader focus of this research on all meltwater types.

Meltwater detection algorithms using microwave signals allow for studying the seasonal variations of backscatter intensity and brightness temperature, as observations are also retrieved during winter [see Fig. 1(c)]. For C-band active microwave sensors, Ashcraft and Long [63] developed a method that assumed melt when the backscatter intensity is lower than the annual winter mean -3 dB. The threshold of 3 dB aligns well with theoretical results and direct observations [75]. While this approach is widely used for melt detection in Antarctica (e.g., [16], [76], [77]), also other thresholds have been used, e.g., using multiple thresholds [37] or adaptive thresholds [78].

Most passive microwave-based melt detection methods make use of the 19 GHz horizontally polarized channel, since this frequency and polarization show the lowest T_b over dry firn, thereby maximizing the increase in T_b by an increased liquid water content [48]. Already in the 1990s, Zwally and Fiegles [79] developed a method for melt detection over Antarctica using the 19 GHz horizontal channel. They assumed melt to occur when the measured brightness temperature exceeds the annual winter mean by 30 K, similar to the method proposed by Mote et al. [80]

TABLE I
SENSOR PROPERTIES OF THE REMOTE SENSING SENSORS DEPLOYED IN THIS STUDY

Sensor	ASCAT	MODIS	Sentinel-1	SSMIS
Start data coverage	October 2006	February 2000 (Terra) July 2002 (Aqua)	April 2014 (Sentinel-1A) April 2016 (Sentinel-1B)	March 2008 (F17) March 2010 (F18)
Spatial resolution	4.45×4.45 km	250, 500, and 1000 m	IW mode: 5×20 m EW mode: 40×40 m	6.25×6.25 km (19 GHz) 3.125×3.125 km (37 GHz)
Temporal resolution	Twice* a day	Twice a day	Varying	Twice a day
Local overpass time	6:00, 18:00	10:30 (Terra), 13:30 (Aqua)	Varying**	6:00, 18:00

* on alternate days, ** orbit dependent

for melt detection over the Greenland Ice Sheet. We refer to this method as M+30. Torinesi et al. [47] suggested a more advanced method, referred to as M+3S, in which they used a dynamic threshold based on the standard deviation of the T_b signal. In 2002, Ramage and Isacks [81] developed the diurnal amplitude variations (DAVs) method, which has been successfully applied to study surface melt [82], [83], [84]. The high revisit time of twice a day for many passive microwave sensors allows for making use of the difference between the morning and afternoon T_b signal, when melt and subsequent refreezing occurs. Tedesco et al. [82] found that the DAV algorithm reduces the underestimation of surface melt that can exist for the M+30 and M+3S methods. The DAV algorithm works best for the 37 GHz vertically polarized channel, as it is less noisy than the 19 GHz channel [85]. Besides the M+30, M+3S, and DAV algorithms, other studies applied statistical K-means clustering [76] and the cross-polarization (horizontal and vertical) gradient ratio of the 19 and 37 GHz frequencies [86] for surface melt detection.

III. DATA

A. Study Area

In this study, we assessed the spatiotemporal melt patterns on a continental scale, but specifically focused on four regions over which meltwater has been detected in previous studies: 1) the Amery Ice Shelf; 2) Roi Baudouin Ice Shelf; 3) Shackleton Ice Shelf; and 4) the Antarctic Peninsula (among others Larsen B and C, George VI, and Wilkins ice shelves) (see Fig. 3).

B. Satellite Imagery

Data from four widely used sensors (i.e., ASCAT, MODIS, Sentinel-1, and SSMIS) were acquired and preprocessed using the Google Earth Engine [87]. Table I provides an overview of the properties of the four sensors.

The ASCAT data with an enhanced resolution (i.e., 4.45 km) and vertical polarization, developed by the NASA Scatterometer Climate Record Pathfinder Project [88], were downloaded from Brigham Young University Microwave Earth Remote Sensing Laboratory¹. Over dry snowpacks in the interior of the Antarctic Ice Sheet, the backscatter intensity is very weak, due to deep penetration of the microwave signals [89]. These low signal-to-noise pixels were therefore masked. We followed Zheng and

Zhou [90] and assumed a low signal-to-noise ratio when a pixel fulfilled one of the following conditions.

- 1) The winter (June–August) mean was lower than -14 dB.
- 2) The minimum winter backscatter intensity was less than 3 dB smaller than the minimum summer (December–February) backscatter intensity.

For MODIS, the MOD09GA (MODIS/Terra Surface Reflectance Daily L2G Global 1 km and 500 m SIN Grid) and MYD09GA (MODIS/Aqua Surface Reflectance Daily L2G Global 1 km and 500 m SIN Grid) products were acquired and combined into daily composites based on the least cloudy observation. This dataset provides a daily visible and near-infrared reflectance over the Antarctic Ice Sheet in which cloud pixels were masked out according to the *1-km Reflectance Data State QA* band.

This study used Sentinel-1 Level-1 ground range detected (GRD) scenes available in Google Earth Engine where they were preprocessed using the Sentinel-1 toolbox to generate a calibrated, orthorectified product [87]. All available horizontally polarized GRD scenes over the Antarctic Ice Sheet for the five melt seasons were selected, giving a combination of interferometric wide (IW) and extra wide (EW) overpasses for which the melt detection algorithm was applied per orbit. Similar to ASCAT, pixels with a low signal-to-noise ratio in the interior of the Antarctic Ice Sheet were masked.

For SSMIS, two melt detection algorithms were implemented: 1) M+3S (abbreviated to $SSMIS_{M+3S}$); and 2) DAV (abbreviated to $SSMIS_{DAV}$), with each algorithm requiring different input data. The $SSMIS_{M+3S}$ results were computed using horizontally polarized 19 GHz observations with a spatial resolution of 6.25 km, the finest enhanced resolution product available for the 19 GHz frequency. Observations from platform F17 were ingested, which has the highest orbit stability². The $SSMIS_{DAV}$ algorithm gives best results for vertically polarized 37 GHz observations [85]. Observations with a spatial resolution of 3.125 km were used, the finest spatial resolution for the 37 GHz frequency. The vertically polarized 37 GHz data of platform F17 are corrupted from April 2016 onward. Therefore, data from the F18 platform were used instead, which have a lower orbit stability than data from the the F17 platform, but nevertheless a similar overpass time as platform F17 when averaged over the

¹Accessed: Apr. 4, 2022. [Online]. Available: <http://www.scp.byu.edu>

²Accessed: Aug. 31, 2022. [Online]. Available: <http://www.remss.com/support/crossing-times/>

study period. All SSMIS observations were obtained from the National Snow and Ice Data Center (NSIDC)³.

C. Weather Stations

Three hourly 2 m air temperature observations from AWS14, located at the Larsen C Ice Shelf, were used. The daily minimum and maximum values were selected and compared to the satellite observations and derived melt predictions. We used the temperature observations to interpret the disagreement between the sensors in detected melt over AWS14. Even though surface temperatures below freezing point can occasionally also lead to melt [91], the positive air temperatures from the weather station were used as first indication for melt presence, similar to many studies (e.g., [37], [45], [92], [93]).

D. Precipitation Data

Precipitation data from RACMO version 2.3p2, which are dynamically downscaled ERA-5 [23], were compared to the detected melt of the four remote sensing satellites. Surface melt can turn into near-surface melt after a snowfall event [94], and therefore remain unnoticed by MODIS. For that reason, we examined whether precipitation events could explain some of the disagreement in detected melt between MODIS and the other three satellites.

E. Sea Ice Concentration

The global 4 km sea ice concentration product PFV53 (AVHRR Pathfinder Sea Surface Temperature Version 5.3), available in the Google Earth Engine [95], was compared to SSMIS_{M+3S} observations. The large measurement response function of SSMIS 19 GHz, with a footprint of ~ 72 by ~ 44 km [96], means that the reported T_b may be contaminated by the pixel surroundings. In the case of a near-coastal pixel surrounded by open water, the effect on the T_b observation can be large, since open water has a very low T_b compared to (sea) ice.

The allocated sea ice concentration for a near-coastal SSMIS pixel was presumed to be the average sea ice concentration of all ocean pixels in the buffering area with a radius of 58 km around the pixel of interest, corresponding to the mean of the measurement response function.

F. Contour Lines

The grounding line, coastline, and outlines of the ice shelves were obtained from the NSIDC MEaSURES campaign created between 2007 and 2009 [97]. The outlines of the individual ice shelves were clipped using the more up-to-date coastline product of the British Antarctic Survey from 2021 [98]. Finally, we used a digital elevation model of Antarctica based on CryoSat-2 observations between July 2010 and July 2016 [99] to eliminate elevations over 1700 m (similar to, e.g., [100]) at which melt is not expected.

IV. METHODS

A. Melt Detection Methods

We computed the binary melt presence, i.e., $m(t)$ (0: no melt, 1: melt), for the four studied remote sensing sensors using state-of-the-art melt detection algorithms. We focused on austral summers (December, January, and February) for five melt seasons, between (December) 2015 and (February) 2020.

Since both ASCAT and Sentinel-1 are C-band sensors, the same widely used melt detection algorithm was applied, proposed by Ashcraft and Long [63]. Melt presence is assumed when the backscatter intensity is smaller than the annual winter mean minus a certain threshold by using

$$m(t) = \begin{cases} 1, & \sigma^0(t) < \sigma_{\text{winter}}^0 + \Delta\sigma^0 \\ 0, & \sigma^0(t) \geq \sigma_{\text{winter}}^0 + \Delta\sigma^0 \end{cases} \quad (1)$$

where σ_{winter}^0 is the average backscatter intensity of the previous winter (June–August) months and $\Delta\sigma^0$ is the threshold which is set to -3 dB. Sentinel-1 observations were processed on a per relative orbit basis.

For MODIS, we used the NDWI_{ice} to detect meltwater. Over Antarctica, different thresholds are used for detecting supraglacial lakes, e.g., greater than 0.25 [16], [72], [73], [101], slush, e.g., greater than 0.12 [30], [72], and meltwater, e.g., greater than 0.07 [16]. In this study, we lowered the NDWI_{ice} threshold to 0.05 to include more potentially wet pixels, according to the spectral measurement of wet snow from Hannula and Pulliainen [102]. Melt is assumed when a pixel agreed with the following equation:

$$m(t) = \begin{cases} 1, & \text{NDWI}_{\text{ice}}(t) > 0.05 \\ 0, & \text{NDWI}_{\text{ice}}(t) \leq 0.05 \end{cases} \quad (2)$$

where NDWI_{ice} is the normalized difference between the observed surface reflectance in red and blue bands [$\text{NDWI}_{\text{ice}} = (\text{BLUE} - \text{RED})/(\text{BLUE} + \text{RED})$].

For SSMIS observations, we applied two melt detection algorithms: 1) SSMIS_{M+3S}; and 2) SSMIS_{DAV}. The SSMIS_{M+3S} algorithm, developed by Torinesi et al. [47], is comparable to the active microwave algorithm, as it is also based on the annual winter mean plus a certain threshold. Torinesi et al. [47] proposed a three-step approach to define a threshold. When the brightness temperature exceeds the winter mean plus the derived threshold, melt is assumed, using

$$m(t) = \begin{cases} 1, & T_b(t) > T_{b,\text{winter}} + \Delta T_b \\ 0, & T_b(t) \leq T_b + \Delta T_b \end{cases} \quad (3)$$

where ΔT_b is the threshold which is set to at least 30 K, but can be as large as three times the standard deviation [46]. The standard deviation is obtained by computing the mean T_b over all observations of a melt year (from April 1 to March 31), then excluding all observations exceeding the mean by at least 30 K, and repeating this process in three iterations. In this way, the high brightness temperatures are removed, and the standard deviation is computed using the filtered dataset.

The second algorithm applied to SSMIS observations, referred to as SSMIS_{DAV}, makes use of the difference between

³Accessed: Apr. 14, 2022. [Online]. Available: <http://www.nsidc.org>

morning and afternoon T_b . The method was first used by Ramage and Isacks [81] over Alaska. Zheng et al. [84] found that a threshold of 9 K was optimal for detecting surface melt over the Antarctic Ice Sheet. According to the SSMIS_{DAV} algorithm, melt is assumed when a pixel agreed with the following equation:

$$m(t) = \begin{cases} 1, & |T_{b,\text{morning}}(t) - T_{b,\text{afternoon}}(t)| > \Delta\text{DAV} \\ 0, & |T_{b,\text{morning}}(t) - T_{b,\text{afternoon}}(t)| \leq \Delta\text{DAV} \end{cases} \quad (4)$$

where $T_{b,\text{morning}}$ and $T_{b,\text{afternoon}}$ are the brightness temperature of the morning and afternoon overpasses, respectively, and ΔDAV equals 9 K.

B. Sensitivity Studies

Multiple sensitivity studies were applied to assess the differences in detected melt for the four sensors. Our sensitivity analyses consisted of four parts: 1) spatiotemporal sensitivity; 2) overpass time sensitivity; 3) sensitivity to liquid water; and 4) melt detection algorithm sensitivity.

1) *Spatiotemporal Sensitivity*: Once the surface melt was detected in the satellite observations, we compared the results in both spatial and temporal domains. To study the spatial patterns, we calculated a summer melt occurrence (SMO; in percentage), a statistical representation to intercompare the detected melt, using

$$\text{SMO} = \frac{\# \text{ melt}}{\# \text{ observations}} \times 100 [\%] \quad (5)$$

in which the number of melt observations (# melt) and the total number of observations (# observations) were computed per pixel. To calculate the # melt, we summed all the observations for which melt was detected over the five studied melt seasons, using the state-of-the-art melt detection algorithms, as described in Section IV-A. We computed the # observations by summing all the available observations over the studied melt seasons. An SMO of 0% means that there was no melt observed over the studied period, whereas an SMO of 100% holds that over all the observations melt was detected.

For ASCAT, Sentinel-1, and SSMIS, we used all the observations. For MODIS, SMO was solely calculated based on cloud-free pixels. While the role of clouds on melt is still under debate, clouds alter the shortwave/longwave energy budget, which could lead to (additional) melting [69], [103], [104], [105], [106]. Therefore, MODIS likely underestimates melt in cloudy regions, preventing an unbiased comparison between MODIS and the other sensors.

For the temporal analysis, time series were created to analyze the satellite signals over seven locations. These locations were selected based on their large difference in SMO between the sensors. For all the points, we compared both the input signals in the used melt detection algorithms (i.e., σ^0 , NDWI_{ice} , and T_b) as the derived melt. Again, note that, especially for optical imagery, this can lead to biased results, as surface melt is possibly correlated to cloudiness.

2) *Overpass Time Sensitivity*: To assess the sensitivity of the melt detection algorithms to overpass time, we analyzed the SMO for both ASCAT and SSMIS_{M+3S} for morning and afternoon observations separately. This analysis was performed

over the four study areas described in Section III-A where for the Antarctic Peninsula only the ice shelf pixels were analyzed.

Since for Sentinel-1 and MODIS no balanced morning and afternoon datasets were available, the overpass time sensitivity analysis was not applied to these datasets. In case of Sentinel-1, the overpass times are orbit-dependent and vary largely throughout the continent. For example, over the Larsen C Ice Shelf, 58% of the observations were captured in the early morning (3 AM–6 AM) and only 42% in the evening (6 PM–9 PM). Also MODIS does not have the same amount of cloud-free morning (10:30 AM) as afternoon (1:30 PM) observations. Since the cloud cover changes frequently over the Antarctic Ice Sheet, the number of Aqua and Terra observations differ depending on the time of the year [107]. Finally, melt results from SSMIS_{DAV} were not studied for the overpass time sensitivity analysis, because the algorithm combines the morning and afternoon observations into one daily melt product.

3) *Sensitivity to Liquid Water*: The Snow Microwave Radiative Transfer (SMRT) [108] model was used to study the sensitivity of microwave sensors to the presence of liquid water. SMRT is a 1-D model that simulates the interaction of microwave signals with a stack of horizontal layers, each with its specific properties (such as density, temperature, and liquid water) [108], [109]. Similar to the work of Picard et al. [109], the exponential representation was selected to model the microstructure of the snowpack. This representation assumes an exponential function for the correlation function, therefore information about the grain size did not have to be provided, and only the correlation length of each layer was required. The implemented model framework was similar to other SMRT studies [108], [109], [110]. The improved Born approximation (IBA) theory [111] was selected to compute the scattering and absorption coefficients per layer, and the radiative transfer equation for the whole snowpack was solved according to the discrete ordinate and eigenvalue (DORT) method [108].

The SMRT model was used to simulate the backscatter intensity of ASCAT and Sentinel-1, and brightness temperature of SSMIS, for a snowpack with varying liquid water contents. The sensitivity of the sensors to liquid water was assessed with the following sensor settings: ASCAT (frequency: 5.4 GHz; polarization: VV; and incidence angle: 40°), Sentinel-1 (frequency: 5.2 GHz; polarization: HH; and incidence angle: 40°), SSMIS for the SSMIS_{M+3S} algorithm (frequency: 19 GHz; polarization: H; and incidence angle: 55°), and SSMIS for the SSMIS_{DAV} algorithm (frequency: 37 GHz; polarization: V; and incidence angle: 55°). The default snowpack parameters for the upper layer (i.e., snow), middle layer (i.e., firn), and bottom layer (i.e., ice) are given in Table II. The sensitivity of these parameters (i.e., thickness, density, correlation length, and temperature) was assessed by adjusting them one by one.

4) *Melt Detection Algorithm Sensitivity*: Since the assessed melt detection algorithms rely on thresholds to derive a binary estimate (i.e., melt or no melt), we evaluated the sensitivity of the selected thresholds by comparing the SMO for different thresholds. This is important because smaller thresholds result in more melt, as smaller deviations are classified as melt, whereas larger thresholds result in less melt. To assess the threshold

TABLE II
DEFAULT SNOWPACK PARAMETERS FOR SMRT SIMULATIONS

	Upper layer <i>snow</i>	Middle layer <i>firn</i>	Bottom layer <i>ice</i>
Thickness (m)	0.1	10	100
Density (kg/m ³)	200	600	900
Correlation length (m)	1e-4	5e-4	6e-4
Temperature (K)	270	250	240

sensitivity (TS), we varied the thresholds applied in (1)–(3). For ASCAT and Sentinel-1, we varied $\Delta\sigma^0$ from -5 to -1 dB with steps of 0.1 dB. For MODIS, we varied the threshold of $NDWI_{ice}$ for melt detection from 0 to 0.1 with steps of 0.01. For $SSMIS_{M+3S}$, we varied ΔT_b from 20 to 40 K with steps of 1 K. The ΔDAV threshold applied in the $SSMIS_{DAV}$ algorithm was varied from 5 to 13 K with steps of 0.1 K.

Then, for each sensor, we selected the thresholds that resulted in 10% more summed melt pixels compared to the default thresholds, which we defined as $SMO_{10\%}^+$. The same method was repeated to obtain the thresholds that resulted in 10% less melt, which we defined as $SMO_{10\%}^-$. Finally, the TS was computed using

$$TS = SMO_{10\%}^+ - SMO_{10\%}^- \quad (6)$$

in which TS is a value between 0 and 100%. When TS equaled 0%, the melt occurrence for a pixel was insensitive for the threshold, and the same SMO was obtained for the small and large thresholds. For larger TS values, more melt was computed using the small threshold than for the large threshold.

V. RESULTS

A. Data Availability

Fig. 2 shows the data availability of the four sensors over the examined melt seasons. The results indicate large differences in the number of observations for each sensor.

ASCAT has almost complete coverage over the entire Antarctic Ice Sheet, with accurate parameter retrieval to $\sim 88^\circ$ south. However, there are some data gaps in the ASCAT dataset, i.e., 22 days in the melt season of 2017–2018 and 30 days in melt season 2018–2019, are missing. Most of the data are missing over West Antarctica and Dronning Maud Land, resulting in ~ 450 overpasses in melt seasons 2015–2020, whereas over Victoria Land and Wilkes Land in East Antarctica ~ 600 observations can be studied. Besides periods of data gaps, ASCAT overpasses twice a day (~ 6 AM, ~ 6 PM local time) on alternating days.

MODIS has frequent coverage over the interior of Antarctica with approximately 400 acquisitions during the study period. However, over the ice shelves, MODIS is severely impacted by cloud cover. The Antarctic Peninsula is especially affected by the persistent clouds. Over Larsen C $\sim 85\%$ of the observations are unusable, as they are covered by clouds, translating to only 66 observations for the five melt seasons, equivalent to an observation once every week.

Similar to MODIS, the number of observations for Sentinel-1 varies strongly between the interior of the Antarctic Ice Sheet and ice shelves. Sentinel-1 retrieves more observations over the

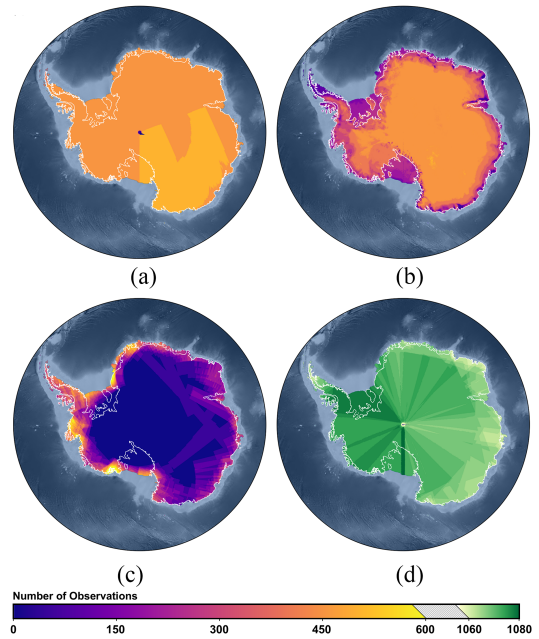


Fig. 2. Number of overpasses over the austral melt seasons 2015 to 2020 for the following. (a) ASCAT. (b) MODIS. (c) Sentinel-1. (d) SSMIS. The number of overpasses for SSMIS shown in subpart (d) are based on the observations of the F17 platform for the horizontally polarized 19 GHz channel (used for $SSMIS_{M+3S}$). SSMIS observations from the vertically polarized 37 GHz channel from the F18 platform (used for $SSMIS_{DAV}$) have a comparable number of overpasses (1082, without data gaps).

ice shelves than over the interior of the ice sheet, as Sentinel-1 is a right-viewing satellite. Over the Antarctic Peninsula, there are ~ 450 overpasses, translating to more or less one overpass per day. The Sentinel-1 mission plan prescribes storing fewer observations over ice shelves in East Antarctica compared to West Antarctica, with ~ 200 overpasses over Amery, Roi Baudouin, and Shackleton ice shelves, translating to ~ 1 overpass every 2–3 days.

SSMIS has the highest overpass frequency, with ~ 1060 overpasses in total in East Antarctica and ~ 1080 in West Antarctica, for the 19 GHz horizontally polarized observations (used for the $SSMIS_{M+3S}$ algorithm). The difference in overpass frequency is a result of some rare failures mostly influencing East Antarctica. For the $SSMIS_{DAV}$ algorithm, for which 37 GHz vertically polarized observations were used, there is an overpass frequency of 1082 over the entire Antarctic Ice Sheet. It should be noted that the $SSMIS_{DAV}$ algorithm combines a morning and an afternoon overpass for one melt observation; hence, the total number of melt observations equals 541 for the study period.

B. Spatiotemporal Sensitivity

Fig. 3 shows the spatial pattern of SMO for melt seasons from 2015 to 2020 over the Antarctic Ice Sheet and the four selected study regions. To further demonstrate the differences in melt detection between the sensors, we present the discrepancies in Fig. 4.

When comparing the SMO of ASCAT to the other sensors, we find large variation over blue ice regions. The blue ice region

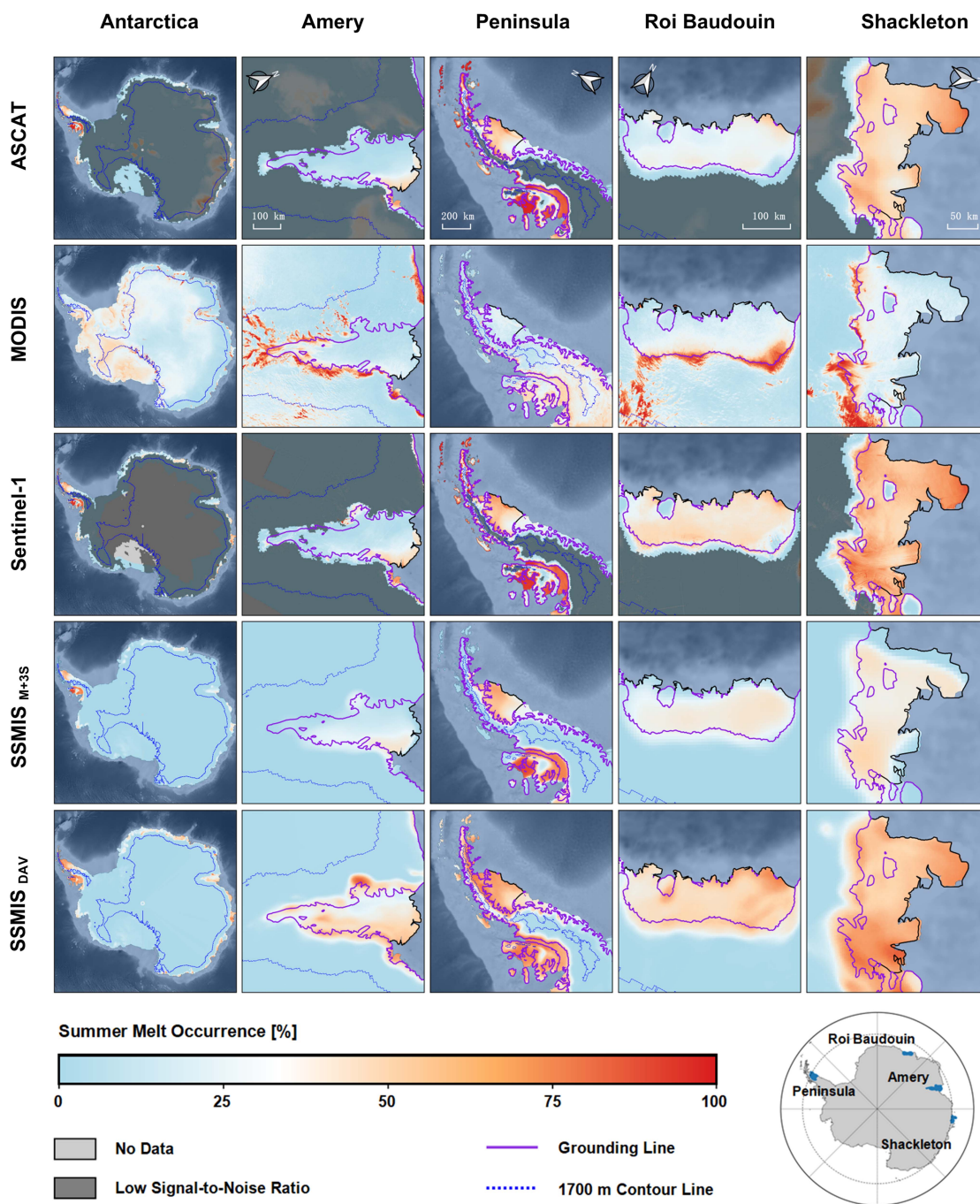


Fig. 3. Melt occurrence for melt seasons 2015–2020 for ASCAT, MODIS, Sentinel-1, and SSMIS over the Antarctic Ice Sheet and four selected ice shelves. For SSMIS, two melt detection methods were applied, i.e., SSMIS_{M+3S} and SSMIS_{DAV}. The light gray areas have no overpasses for the study period. The dark gray areas in ASCAT and Sentinel-1 highlight the low signal-to-noise ratio areas in which the algorithm is unreliable.

located on the south-east of the Roi Baudouin Ice Shelf is the most clear example. At the location indicated with point *a* in Fig. 4, ASCAT detects an SMO of 11%, whereas an SMO of 84%, 25%, and 43% are found for MODIS, SSMIS_{M+3S}, and SSMIS_{DAV}, respectively. Similar to ASCAT, also Sentinel-1 detects a low SMO of 12% over point *a*.

Large discrepancies between MODIS and the other sensors occur both over the center of the ice shelves and along the grounding lines. Over the center of the ice shelves, most of the MODIS observations are cloud-covered (see Fig. 2); therefore,

the SMO was computed on a limited number of observations. MODIS detects an SMO of around 25% over the ice shelves, whereas the other sensors detect an SMO of at least 50% over the studied ice shelves.

On the contrary, MODIS results show an SMO exceeding 75% over the grounding lines of the Amery Ice Shelf, Roi Baudouin Ice Shelf, and Shackleton Ice Shelf, whereas the other sensors detect a lower SMO around 50%. These areas coincide with the blue ice areas as found by Winther et al. [112]. Over the location indicated with point *b* in Fig. 4, MODIS detects an average SMO

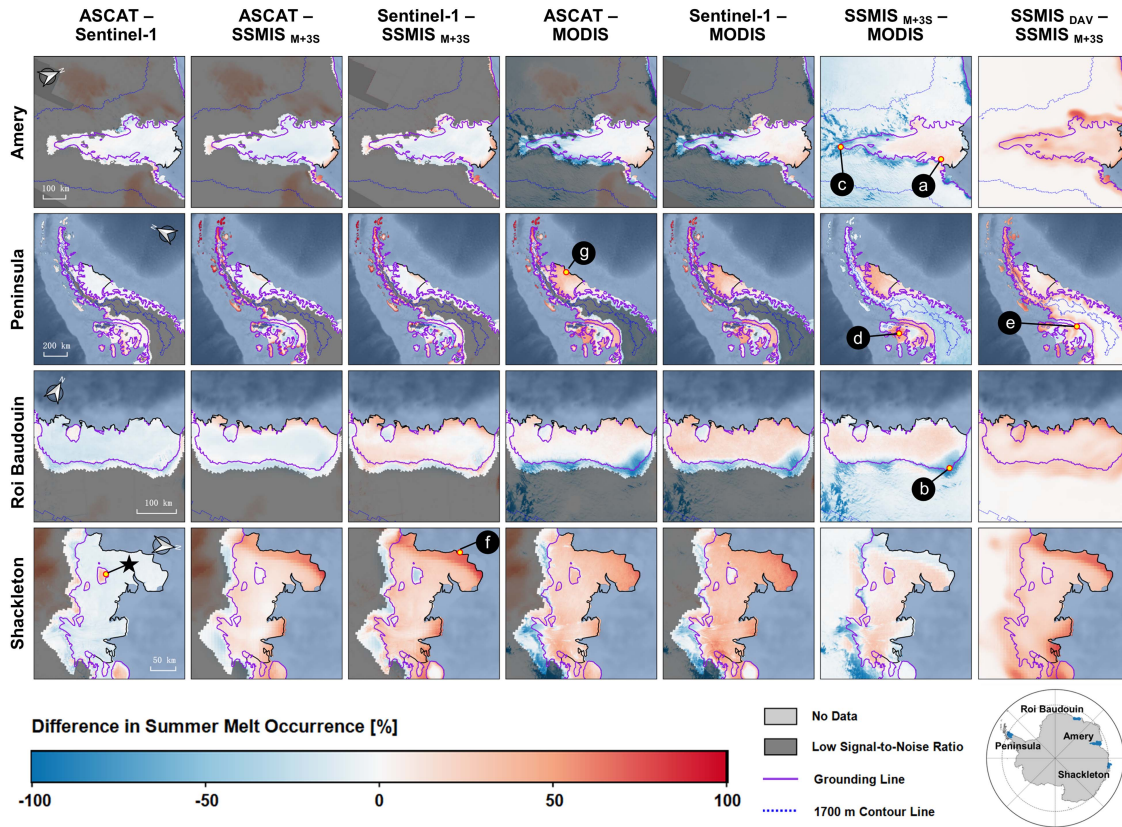


Fig. 4. Difference in melt occurrence for melt seasons 2015–2020 between ASCAT, MODIS, Sentinel-1, and SSMIS over the four selected ice shelves. For SSMIS, two melt detection methods were applied, i.e., $SSMIS_{M+3S}$ and $SSMIS_{DAV}$. The results of $SSMIS_{M+3S}$ are compared to the other three sensors and the last column compares $SSMIS_{M+3S}$ and $SSMIS_{DAV}$. The following seven locations are selected for further analysis. (a) Blue ice. (b) Outlet glacier. (c) Firm aquifer. (d) Snowfall. (e) Winter melt. (f) Near-shore. (g) Persistent melt. The location indicated with a black star is discussed in the text.

of 74%, whereas the SMO equals to 20% for MODIS, 7% for Sentinel-1, 0% for $SSMIS_{M+3S}$, and 9% for $SSMIS_{DAV}$. Due to the optical nature of MODIS, there are differences in SMO between MODIS and the other sensors over regions with near-surface melt, such as over a firm aquifer (point *c* in Fig. 4) and surface melt covered by snowfall (point *d* in Fig. 4). Also, winter melt events are missed by MODIS (point *e* in Fig. 4).

Sentinel-1—with the finest spatial resolution of the four studied sensors—captures more detailed melt features than the other sensors. This is clearly visible for the most northern ice rise at the Shackleton Ice Shelf (indicated with a black star in Fig. 4) that has an average elevation of 300 m. ASCAT and SSMIS (both $SSMIS_{M+3S}$ and $SSMIS_{DAV}$), with a coarser spatial resolution, detect a similar SMO over the ice rise as over the surrounding pixels, with values between 30% and 35% melt. A much lower SMO for Sentinel-1 is found over the ice rise, corresponding to an average SMO of 4%. Such a low SMO value would be expected at higher (and thus colder) elevations.

$SSMIS_{M+3S}$ differs from the other sensors over some near-coast regions. For example, at the pixels near the coast at the western part of Shackleton (the pixels surrounding point *f* in Fig. 4), $SSMIS_{M+3S}$ does not detect any melt. Over this location $SSMIS_{M+3S}$ has an SMO of 0%, whereas a higher SMO is found for ASCAT, MODIS, Sentinel-1, and $SSMIS_{DAV}$ with values of 62%, 14%, 70%, and 69%, respectively.

$SSMIS_{DAV}$ shows a low SMO over areas with persistent melt. An example is the George VI Ice Shelf on the Antarctic Peninsula, with an average SMO of 55% over point *g* in Fig. 4, whereas values of 80%, 77%, and 72% are detected by ASCAT, Sentinel-1, and $SSMIS_{M+3S}$, respectively. Again, also MODIS results in a lower SMO (i.e., 41%) over the often clouded George VI Ice Shelf.

To better understand the discrepancies and similarities between the sensors, the time series of seven locations were compared. The locations of points *a*–*g* can be found on the maps of Fig. 4. The satellite signals and detected melt over these locations are shown in Fig. 5.

Fig. 5(a) and (b) show that there are large discrepancies in melt detection over bare ice regions, such as a blue ice area and an outlet glacier. MODIS detects more melt over the blue ice location [see Fig. 5(a)] (95%) than ASCAT (32%), Sentinel-1 (31%), $SSMIS_{M+3S}$ (18%), and $SSMIS_{DAV}$ (66%) in melt seasons 2019–2020. Also, over the outlet glacier [see Fig. 5(b)], more melt is detected by MODIS (100%) than by ASCAT (30%), Sentinel-1 (33%), $SSMIS_{M+3S}$ (6%), and $SSMIS_{DAV}$ (19%), here computed for melt seasons 2016–2017. MODIS detects a persistently high $NDWI_{ice}$ over the bare ice regions [0.10 for Fig. 5(a); 0.16 for Fig. 5(b)], resulting in detected melt for (almost) all observations. On the other hand, almost no drop in backscatter intensity of ASCAT and Sentinel-1 is visible

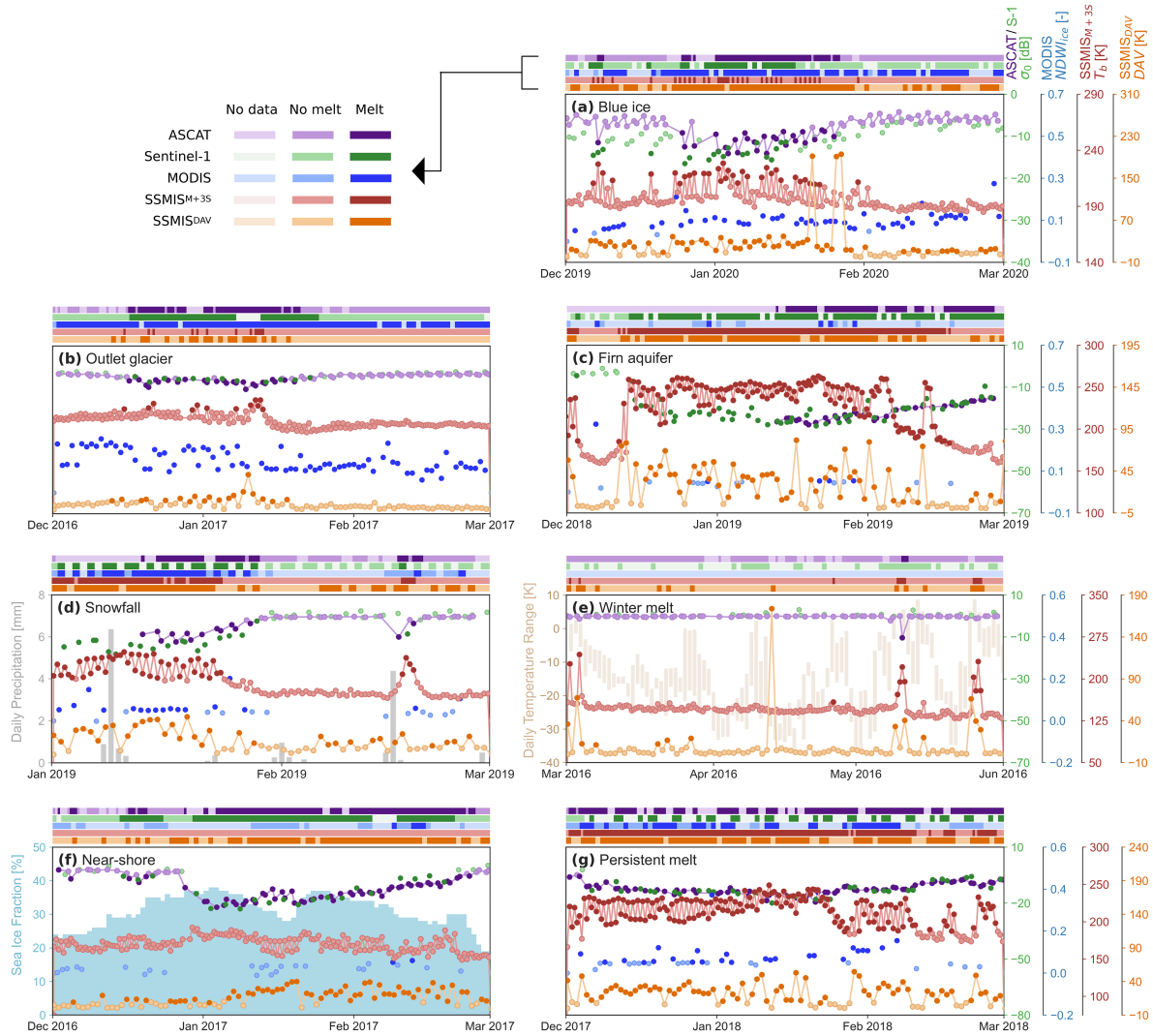


Fig. 5. Time series of backscatter intensity (σ^0), NDWI_{ice}, brightness temperature (T_b), and DAV for the four studied sensors. The comparison shows the measured σ^0 of ASCAT (in purple), σ^0 of Sentinel-1 (in green), NDWI_{ice} of MODIS (in blue), T_b of SSMIS SSMIS_{M+3S} (in red), and DAV for SSMIS_{DAV} (in orange). When melt is detected, the signals are overlaid with a darker scatter. The flags on top of each subfigure facilitate intercomparison of the melt results, indicating no data (light color), no melt (medium color), and melt (dark color); see the legend in the left upper corner for the specific colors used per melt detection method. The locations of (a)–(g) are shown in Fig. 4.

during the melt seasons relative to winter period values, and no clear peak presents in the brightness temperature of SSMIS, explaining the less frequent melt detection by the microwave sensors.

Fig. 5(c) illustrates the sensor signals over a firm aquifer (subsurface meltwater stored in pore spaces in the firm layer) at the Wilkins Ice Shelf. Montgomery et al. [113] detected a firm aquifer here, starting at 13.4 m depth with a total thickness of 16.2 m in December 2018, which indicates that the climatic conditions are in general favorable for liquid water storage below the surface. ASCAT and Sentinel-1 detect melt for the longest period (up to April 2019) over this location, which may hint on the detection of near-surface melt instead of surface melt, as ASCAT and Sentinel-1 have relatively large penetration depths. Both SSMIS_{M+3S} and SSMIS_{DAV} detect melt for a shorter period than ASCAT and Sentinel-1, until mid-February. MODIS

only detects melt during the end of December and January, thereafter no melt is detected.

We also see differences in melt detection after snowfall events [see Fig. 5(d)], potentially also due to confusion between surface and near-surface melt. Again, MODIS only measures surface melt, therefore it fails to detect melt covered by snow after precipitation events (January 11 and February 15), whereas other sensors do detect (near-surface) melt.

Since MODIS depends on reflected sunlight, no melt observations can be performed during the winter season. However, there are locations in Antarctica where up to 20% to 25% of the melt occurs during the winter season, driven by foehn winds [20]. Fig. 5(e) shows an example of such a winter melt event (reported in [41]). Both SSMIS_{M+3S} and SSMIS_{DAV} detect melt during the three periods of elevated temperature, in the beginning of March, mid-May, and end of May. ASCAT detects melt once,

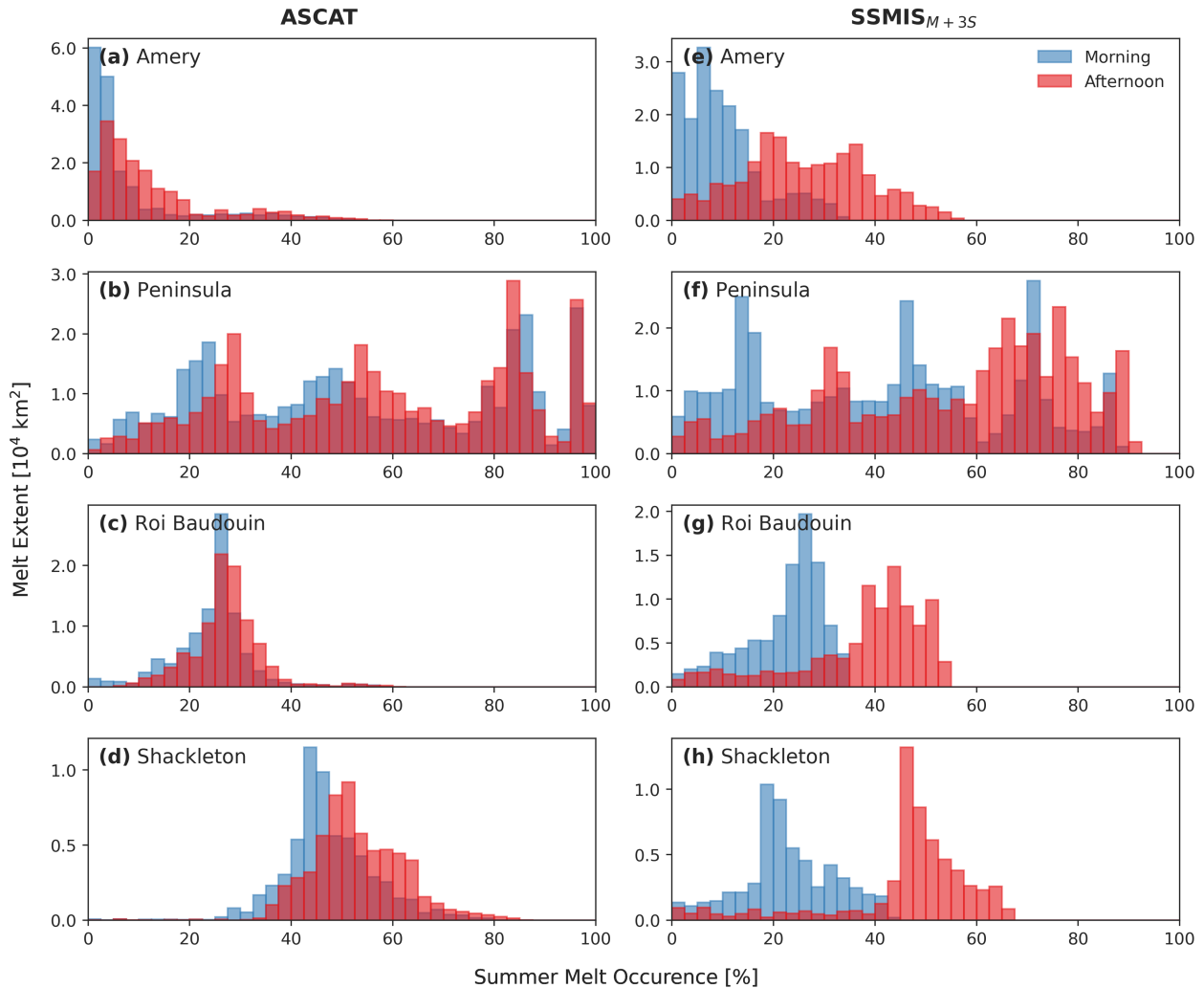


Fig. 6. Melt occurrence for morning and afternoon observations for the following. (a)–(d) ASCAT. (e)–(h) $SSMIS_{M+3S}$.

on May 10 at 6 PM. Sentinel-1 does not detect melt, however there are also no overpasses at times where SSMIS detects melt (i.e., March 1 and 3, May 9–11 and 25–27).

$SSMIS_{M+3S}$ detects no melt during the melt seasons for near-coastal pixels at locations where sea ice strongly decreases during summer. Fig. 5(f) shows that changes in sea ice concentration and SSMIS brightness temperature correspond. When the sea ice concentration decreases (e.g., in the beginning of January 2017), the SSMIS brightness temperature follows. This is because the large footprint of $SSMIS_{M+3S}$ results in mixed pixels where open water masks the increased brightness temperature during melt. For $SSMIS_{DAV}$, this problem is minimized because the 37 GHz has a smaller footprint than the 19 GHz channel and the $SSMIS_{DAV}$ algorithm compensates for the low T_b signal by subtracting morning from afternoon overpasses.

Extensive areas of ponded surface water have been observed over the northern part of the George VI Ice Shelf since the early 1940s [100], [114], [115]. Where ASCAT, Sentinel-1, and $SSMIS_{M+3S}$ detect melt of 99%, 97%, and 85%, respectively, averaged over melt seasons 2017–2018, this is lower for $SSMIS_{DAV}$ (i.e., 72%), as shown in Fig. 5(g). The applied $SSMIS_{DAV}$ algorithm detects melt when the difference between

morning and afternoon observations exceeds 9 K; however, for areas with persistent melt throughout the summer, the difference between morning and afternoon observations are too small to pass this threshold.

C. Overpass Time Sensitivity

When we compare the SMO for morning and afternoon overpasses for ASCAT and $SSMIS_{M+3S}$ in Fig. 6, afternoon observations show higher SMO than morning observations with differences of 16% (4%) over Amery Ice Shelf, 15% (3%) over the Antarctic Peninsula, 14% (4%) over Roi Baudouin Ice Shelf, and 23% (6%) over Shackleton Ice Shelf for $SSMIS_{M+3S}$ (for ASCAT between brackets). This shows that the overpass time can have a large influence on the detected melt.

The differences between ASCAT and $SSMIS_{M+3S}$ are small for morning observations. However, $SSMIS_{M+3S}$ detects more melt than ASCAT during afternoon observations. The Antarctic Peninsula forms an exception here, where meltwater is abundant also during nighttime (e.g., shown by the small diurnal variation in detected melt over the Antarctic Peninsula in [44]), thereby

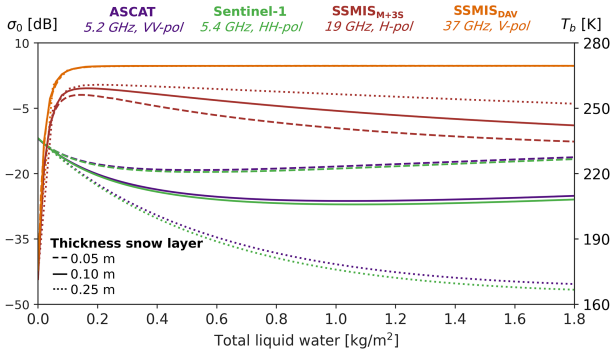


Fig. 7. Modeled backscatter intensity (σ^0) from ASCAT vertically polarized (in purple) and Sentinel-1 horizontally polarized (in green), and brightness temperature (T_b) from SSMIS 19 GHz horizontally polarized (in red) and 37 GHz vertically polarized (in orange) as a function of the total liquid water content in the top 0.05 (dashed lines), 0.10 (solid lines), or 0.25 m (dotted lines) of the snowpack.

explaining the high SMO during both morning and afternoon observations for both sensors.

While we did not assess the influence of overpass time for MODIS and Sentinel-1 due to lack of variations of overpass times, Fig. 5(e) shows how mismatching overpass timing and a lower temporal resolution result in potential missed melt events for Sentinel-1.

D. Sensitivity to Liquid Water

The backscatter intensity and brightness temperature sensitivity to liquid water for different thicknesses of the upper layer are assessed in Fig. 7, the sensitivity to the other three parameters (i.e., density, correlation length, and temperature) are evaluated in Fig. A1. Results from our radiative transfer model SMRT suggest that SSMIS (19 and 37 GHz) is highly sensitive to small liquid water contents. The brightness temperature increases with 80/95 K for 19/37 GHz, respectively, for a total liquid water content of 0.10 kg/m^2 compared to a dry snowpack, with a snow layer thickness of 0.10 m. After reaching a maximum brightness temperature (approximately at a total liquid water content of 0.10 kg/m^2), the brightness temperature slowly decreases because the surface becomes more reflective. The backscatter intensities of ASCAT and Sentinel-1, which slightly differ due to small differences in polarization and frequency, require approximately a ten-fold larger liquid water content (approximately 1.0 kg/m^2) than SSMIS to become fully saturated.

As shown in Fig. 7, the increase in brightness temperature for SSMIS 19 GHz is largest for thicker snow layers (i.e., 75/86 K for 0.05/0.25 m, respectively, when comparing a dry snowpack to a snowpack with a total liquid water content of 0.10 kg/m^2). For SSMIS 37 GHz, the brightness temperatures are (almost) identical for different snow layer thicknesses. For ASCAT and Sentinel-1, the drop in backscatter intensity is small, especially for shallow snow layers (i.e., $-2.5/-7.1$ dB for 0.05/0.25 m, respectively, when comparing a dry snowpack to a snowpack with a total liquid water content of 1.0 kg/m^2) making ASCAT and Sentinel-1 less sensitive to liquid water in shallow snow layers, but also to snow layers with lower densities, larger correlation lengths, and higher temperatures (see Fig. A1).

TABLE III
SUMMARY OF THE PERTURBED THRESHOLDS FOR THRESHOLD SENSITIVITY ANALYSIS

Sensor	Threshold for $\text{SMO}_{10\%}^+$	Threshold for $\text{SMO}_{10\%}^-$
ASCAT	-3.9 (dB)	-2.3 (dB)
MODIS	0.045 (-)	0.055 (-)
Sentinel-1	-4.0 (dB)	-2.4 (dB)
SSMIS _{M+3S}	26 (K)	34 (K)
SSMIS _{DAV}	8.0 (K)	10.4 (K)

The high sensitivity of SSMIS to small liquid water contents might explain the previously observed difference in afternoon SMO between ASCAT and SSMIS_{M+3S} (see Fig. 6). Especially, over the Amery Ice Shelf and Roi Baudouin Ice Shelf, the afternoon observations of SSMIS_{M+3S} show a higher SMO than ASCAT. According to Fig. 6, over Amery Ice Shelf, the difference in SMO is 14% (ASCAT afternoon mean: 12%, SSMIS afternoon mean: 26%) and over Roi Baudouin 11% (ASCAT afternoon mean: 27%, SSMIS_{M+3S} afternoon mean: 38%). This difference can be linked to the small mean surface melt flux over these ice shelves (around 100 mm w.e. year⁻¹), whereas the fluxes are larger over the Antarctic Peninsula and the Shackleton Ice Shelf (between 200–400 mm w.e. year⁻¹ and around 200 mm w.e. year⁻¹, respectively) according to satellite-based estimates [52] and RACMO2 simulations [23].

The higher sensitivity of SSMIS might also explain the discrepancies in Fig. 5(e). Both SSMIS_{M+3S} and SSMIS_{DAV} detect more melt than ASCAT and Sentinel-1 during the melt events in the winter of 2016. However, this might also be linked to the lower overpass frequency of ASCAT and Sentinel-1, as stated in the previous Section V-C.

E. Melt Detection Algorithm Sensitivity

Fig. 8 shows the TS for ASCAT, MODIS, Sentinel-1, SSMIS_{M+3S}, and SSMIS_{DAV}. The used thresholds for $\text{SMO}_{10\%}^+$ and $\text{SMO}_{10\%}^-$ are given in Table III. The highest TS for ASCAT, Sentinel-1, SSMIS_{M+3S}, and SSMIS_{DAV} arise along the grounding lines. Especially for SSMIS_{M+3S} and SSMIS_{DAV}, more melt is detected inward from the grounding line, where we find that on average $\text{SMO}_{10\%}^+$ results in $\sim 10\%$ – 15% more melt than $\text{SMO}_{10\%}^-$. For MODIS, $\sim 15\%$ – 20% more melt is detected over the center of ice shelves when using the $\text{SMO}_{10\%}^+$ threshold. The original threshold of NDWI_{ice} shows a low SMO compared to the other sensors over these regions (see Fig. 3); hence, a lower threshold of NDWI_{ice} might result in more comparable melt results as the other sensors. Nevertheless, areas that showed a relatively high SMO compared to the microwave sensors (see Fig. 3) (i.e., blue ice regions) are less sensitive to the selected threshold and would also overestimate melt presence with an $\text{SMO}_{10\%}^-$ threshold compared to the other sensors.

VI. DISCUSSION

A. Opportunities and Challenges: Perspectives of Sensor Characteristics

Based on the comparison of the detected melt for the four sensors, we identify four opportunities and challenges in relation to the sensor characteristics, including cloud obstruction and

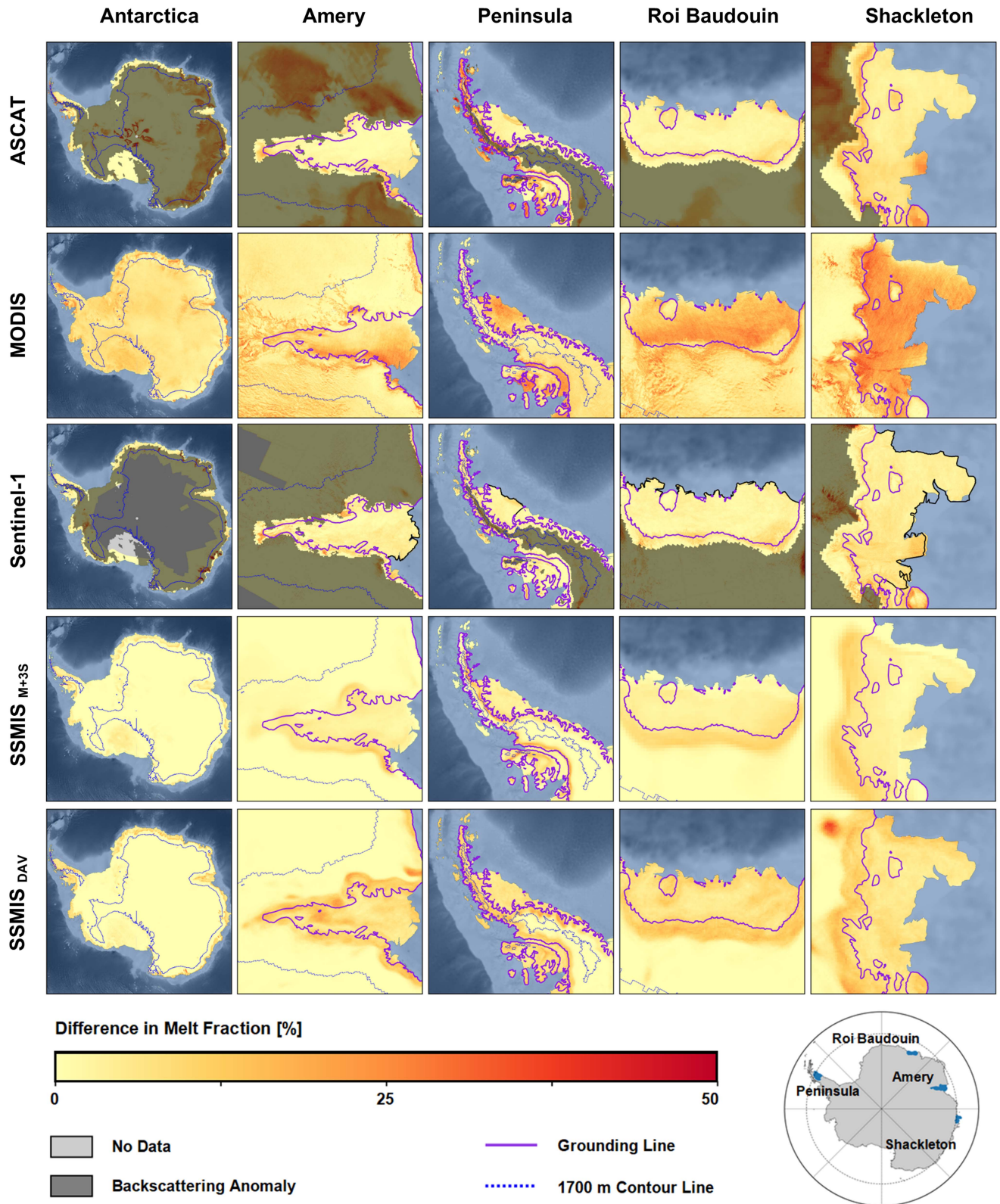


Fig. 8. Melt sensitivity for melt seasons 2015–2020 for ASCAT, MODIS, Sentinel-1, and SSMIS using algorithm SSMIS_{M+3S} and SSMIS_{DAV} over the four selected ice shelves. The difference in melt occurrence is computed by comparing small and large thresholds, compared to the default thresholds used in the state-of-the-art melt detection algorithms.

TABLE IV
SUMMARY OF THE IDENTIFIED ADVANTAGES AND DISADVANTAGES IN DETECTING SURFACE MELT OVER ANTARCTICA USING DIFFERENT REMOTE SENSING SENSORS

	Advantages	Disadvantages
ASCAT * C-band	<ul style="list-style-type: none"> • Overpasses twice a day (on alternate days) • Continental coverage 	<ul style="list-style-type: none"> • Coarse spatial resolution of 4.45 km • Low signal-to-noise ratio over $\sim 75\%$ of the Antarctic Ice Sheet • Fails to detect melt over blue ice • Can confuse surface melt and near-surface melt
MODIS * Blue band * Red band	<ul style="list-style-type: none"> • Fine spatial resolution of 500 m • Daily overpasses over the interior of the Antarctic Ice Sheet (almost always cloud-free) • Almost (daily) overpasses over grounding line (less clouds than over ice shelves) • Captures melt over blue ice regions 	<ul style="list-style-type: none"> • No observations during winter • Between 15%–75% of the observations over ice shelves are cloud-covered during melt season • High threshold sensitivity over center of ice shelves
Sentinel-1 * C-band	<ul style="list-style-type: none"> • Fine spatial resolution of 10–40 m • Almost (daily) overpasses over the West Antarctic ice shelves 	<ul style="list-style-type: none"> • No coverage over interior the Antarctic Ice Sheet • One overpass every two/three days over East Antarctica • Overpass time varies per orbit • Low signal-to-noise ratio over $\sim 75\%$ of the Antarctic Ice Sheet • Fails to detect melt over blue ice • Can confuse surface melt and near-surface melt
SSMIS * K-band * K_a -band	<ul style="list-style-type: none"> • Overpasses twice a day • Continental coverage • High sensitivity to low liquid water contents 	<ul style="list-style-type: none"> • Coarse spatial resolution of 3.125 km (K_a-band) or 6.25 km (K-band) • Can confuse surface melt and near-surface melt

polar darkness, surface penetration, temporal resolution and overpass time, and spatial resolution.

1) *Cloud Obstruction and Polar Darkness*: Our results showed that cloud obstruction and polar darkness are fundamental limitations for optical data. MODIS does not detect winter melt events [see Fig. 5(e)], whereas especially over the Antarctic Peninsula several melt events have been reported during winter [20], [41], [116]. Moreover, MODIS is unable to capture melt events during cloudy days. This is probably one of the main reasons for the underestimation of melt over the ice shelves where clouds are abundant.

2) *Surface Penetration*: Our analysis showed that large differences in SMO between sensors can result from differences in penetration depth. The active and passive microwave sensors receive signals from dry snowpacks to depths of ~ 10 , ~ 2.5 , and ~ 0.5 m for C-band active microwave, K-band passive microwave, and K_a -band passive microwave, respectively. Therefore, microwave sensors are not only detecting surface melt, but also liquid water in deeper layers. At locations where we expect near-surface melt to be present [see Fig. 5(c) and (d)], ASCAT and Sentinel-1 detected more melt than SSMIS. In contrast, MODIS does not penetrate the surface, and therefore gives the opportunity to purely focus on surface melt. Moreover, the different frequencies of active and microwave sensors provide the opportunity to derive the depth of the meltwater. A recent study attempted to discriminate between surface and near-surface melt over the Greenland Ice Sheet using multiple frequencies of passive microwave sensors [49]. When combining optical,

active, and passive microwave signals, an even more detailed profile of meltwater depths might be acquired.

3) *Temporal Resolution and Overpass Time*: Our results showed that melt over Antarctica can occur for very short periods of time. Sentinel-1, which has a lower temporal resolution than ASCAT and SSMIS, missed such short melt events [e.g., as shown in Fig. 5(e)]. We indicated that afternoon overpasses resulted in a higher SMO than morning overpasses (see Fig. 6). Picard and Fily [44] found that when comparing passive microwave sensors, the differences in overpass time has the most significant effect on SMO, more than other characteristics, such as frequency, incidence angle, and spatial resolution. Bevan et al. [38] compared QuikSCAT and ASCAT melt observations and showed that QuikSCAT detected more melt than ASCAT over the Larsen C Ice Shelf, among others due to the preferable overpass time of QuikSCAT (~ 4 PM local time) over ASCAT (~ 6 PM local time). These findings highlight the importance of available sensor observations during noon, when melt over Antarctica is most likely.

4) *Spatial Resolution*: We demonstrated that coarse spatial resolution observations, such as the 4.45 km observations of ASCAT, the 6.25 km observations of SSMIS_{M+3S}, and the 3.125 km observations of SSMIS_{DAV}, failed to detect smaller scale melt features. ASCAT, SSMIS_{M+3S}, and SSMIS_{DAV} detected melt over the small ice rises at Shackleton Ice Shelf (see Fig. 4), opposed to MODIS and Sentinel-1. Besides, in heterogeneous pixels, their coarse spatial resolution leads to mixing up the surface melt signals with signals from sea ice or open water [see

Fig. 5(f)]. As a consequence, coarse spatial resolution sensors might fail threshold-based surface melt detection methods.

B. Opportunities and Challenges: Perspectives of Applied Methods

Apart from sensor-characteristic-related opportunities and challenges, we also identify opportunities and challenges considering the applied methods. We discuss opportunities and challenges related to the sensitivity to the applied thresholds in the melt detection algorithms, the two melt detection algorithms applied to SSMIS, and discuss implications due to the absence of ground truth data.

1) *Meltwater Detection Thresholds*: ASCAT, Sentinel-1, SSMIS_{M+3S}, and SSMIS_{DAV} show the highest TS along the grounding lines, where MODIS has the highest TS over the center of ice shelves. Over locations with a high TS, thorough research is desired to select optimal thresholds. An example is a study by Trusel et al. [37] in which they proposed to use a decision tree method to determine the appropriate $\Delta\sigma^0$. Since they used QuikSCAT data, future research is required to show the applicability of the proposed thresholds to ASCAT and Sentinel-1 data.

We also found areas where MODIS detected an SMO exceeding $\sim 75\%$ (e.g., over blue ice regions), but had a low sensitivity to the selected threshold. Due to the bluish appearance of blue ice regions, the NDWI_{ice}-based detection method is likely to overestimate surface melt over these regions. Moreover, misclassification of aged snow can result in an overestimation of SMO along the grounding lines detected by MODIS. Based on spectral measurements and simulations [117], [118], the NDWI_{ice} of wet snow or aged snow range from 0.05 to 0.1. Therefore, there is a tradeoff between the detection of wet snow and overestimation of melt over aged snow areas. The MODIS melt detection could potentially be refined by including additional constraints (for example, based on snow grain size or blue ice presence) to the melt detection algorithm. Nevertheless, it should be noted that surface melt can occur in these low albedo areas [27], [119], and optical sensors are able to detect surface melt over these areas (albeit an overestimation), whereas blue ice regions are often underestimated or neglected by regional climate models [23] and the melt detection algorithms applied to microwave sensors.

2) *SSMIS Melt Detection Algorithms*: Besides the frequently used M+3S algorithm (i.e., SSMIS_{M+3S}), also the DAV algorithm (i.e., SSMIS_{DAV}) was applied to the SSMIS data in this research. It was possible to also study the daily brightness temperature variations using the DAV algorithm, because SSMIS observes the Antarctic Ice Sheet twice a day with constant local overpass times. Similar to the work of Tedesco et al. [82], it was found that SSMIS_{M+3S} tends to underestimate melt compared to the other sensors for most of the Antarctic Ice Sheet. Therefore, SSMIS_{DAV} is preferred over the SSMIS_{M+3S} algorithm; however, over persistent melt regions [such as Fig. 5(g)], the SSMIS_{DAV} algorithm underestimates melt compared to the other sensors. Here, the difference between morning and afternoon observations is often smaller than 9 K, whereas the individual brightness temperature of morning and afternoon overpasses are high (i.e., exceeding the previous winter mean plus 30 K).

Therefore, it is recommended to extend the SSMIS_{DAV} algorithm, and not only detect melt when DAV exceeds 9 K, but also when the morning and afternoon overpasses both exceed a certain threshold. Tedesco et al. [46] used such a dual-condition approach to detect melt over the Greenland Ice Sheet; however, these thresholds highly underestimate melt over the Antarctic Ice Sheet, so an additional study over Antarctica would be desired.

3) *Limited Ground Truth Data*: Last but not least, validating the SMO results per sensor was hampered by the absence of ground truth data. Therefore, the results could be compared (between sensors and to auxiliary data), but it remained difficult to explain the discrepancies among the results. AWSs provide a way to validate the absolute value at pixel size. However, given the spatial resolution of sensors, the representativeness over a pixel with heterogeneous melt patterns is still difficult to verify, as well as the spatial patterns of surface melt. Moreover, over areas with the largest SMO differences between sensors, such as blue ice regions, there are no AWSs in place yet.

VII. CONCLUSION

In this study, we presented an overview of opportunities and challenges in detecting surface melt over Antarctica. We applied a range of methods to four frequently used sensors: 1) ASCAT; 2) MODIS; 3) Sentinel-1; and 4) SSMIS. The comparison showed large SMO differences, especially over blue ice regions, in the case of near-surface melt, and during winter melt. In this study, we identified five opportunities and challenges when detecting surface melt over Antarctica, which include: 1) cloud obstruction and darkness; 2) surface penetration; 3) temporal resolution; 4) spatial resolution; and 5) the applied melt detection methods. We also summarize the identified opportunities and challenges in Table IV.

Table IV gives that an opportunity for one sensor is often a challenge for another. We foresee a promising future for combining sensors, in particular, by applying machine learning methods. However, there is a need for machine learning methods that can handle the differences in time and space between the satellites. Standard machine learning techniques will not be sufficient to merge the diverge satellite observations.

There are multiple scenarios in which synergizing satellite data can improve mapping of surface melt over the Antarctic Ice Sheet. There are four opportunities for which we foresee that combining satellite data could be beneficial as follows.

- 1) Melt detection over blue ice could be improved by combining MODIS and microwave data.
- 2) MODIS could help separating surface and near-surface melt, due to its inability to penetrate the surface. When one would be interested in near-surface melt, different microwave frequencies could be compared to assess the depth of meltwater.
- 3) Temporal and spatial resolutions could be enhanced, when sensors with different resolutions are combined into one high-resolution melt presence product.
- 4) Machine learning provides the opportunity to combine multiple input features, including multiple satellite observations or auxiliary datasets, which might lead to an improved melt detection product.

In this study, we performed an intercomparison of surface melt detected by four satellites. A more varied collection of ground truth data from AWSs, including sensors for observing liquid water presence in the snowpack, would be required for a thorough validation study.

APPENDIX SUPPLEMENTARY FIGURES

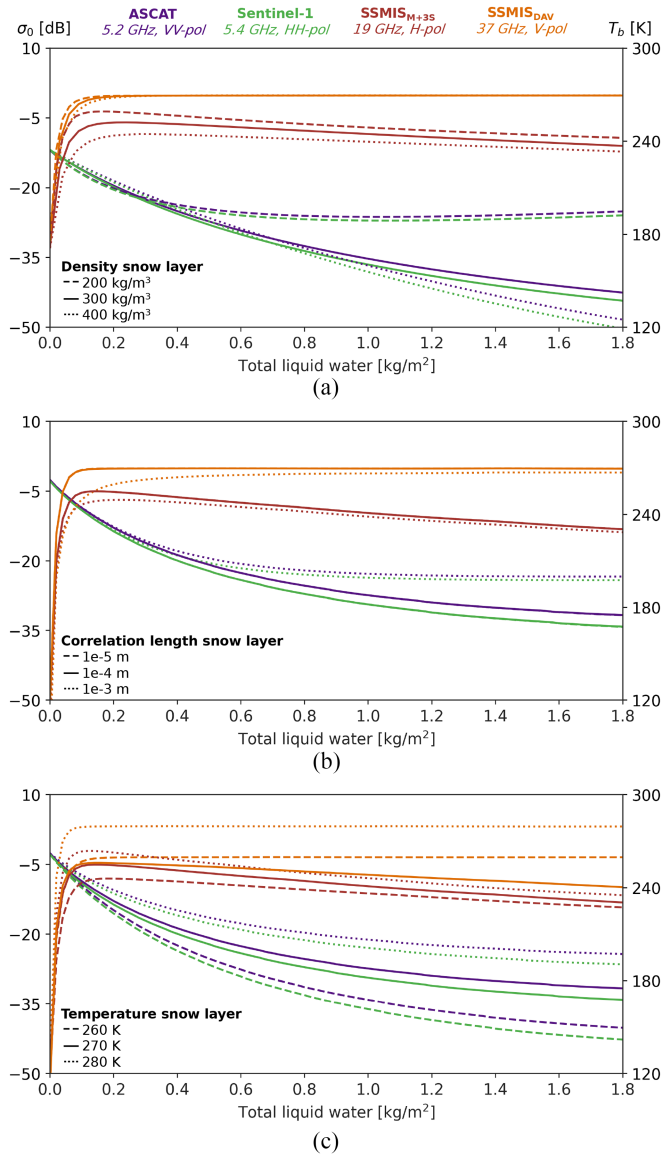


Fig. A1. Modeled backscatter intensity (σ^0) from ASCAT vertically polarized (in purple), and Sentinel-1 horizontally polarized (in green), and brightness temperature (T_b) from Special Sensor Microwave Imager/Sounder 19 GHz horizontally polarized (in red) and 37 GHz vertically polarized (in orange) as a function of the total liquid water content for a varying (a) density, (b) Correlation length, and (c) temperature of the snowpack.

ACKNOWLEDGMENT

The authors would like to thank Prof. Marco Tedesco for his advice on the application of the DAV algorithm applied to

the SSMIS observations, and are grateful for the help of Prof. Ghislain Picard on the application of the SMRT model.

Author contributions: Sophie de Roda Husman designed the research, implemented the analysis (processing satellite data, including ASCAT, Sentinel-1, and SSMIS, processing auxiliary data, and applying sensitivity studies), and wrote the manuscript. Zhongyang Hu designed the research, implemented the analysis (processing satellite data, including MODIS, processing auxiliary data, and applying sensitivity studies), and wrote the manuscript. Bert Wouters, Peter Kuipers Munneke, and Stef Lhermitte designed the research and supported the writing of the manuscript. Sanne Veldhuisen implemented the analysis of RACMO2 data and supported the writing of the manuscript.

REFERENCES

- [1] J. A. Church et al., “Sea level change,” Cambridge Univ. Press, Cambridge, U.K., Tech. Rep., 2013.
- [2] A. M. Bakker, T. E. Wong, K. L. Ruckert, and K. Keller, “Sea-level projections representing the deeply uncertain contribution of the West Antarctic Ice Sheet,” *Sci. Rep.*, vol. 7, no. 1, 2017, Art. no. 3880.
- [3] T. L. Edwards et al., “Projected land ice contributions to twenty-first-century sea level rise,” *Nature*, vol. 593, no. 7857, pp. 74–82, 2021.
- [4] H.-O. Pörtner et al., “Climate change 2022: Impacts, adaptation and vulnerability,” Intergovernmental Panel Climate Change, Geneva, Switzerland, IPCC Sixth Assessment Rep., 2022.
- [5] H.-O. Pörtner et al., “The ocean and cryosphere in a changing climate,” Intergovernmental Panel Climate Change, Geneva, Switzerland, IPCC Special Rep., 2019.
- [6] E. Rignot, J. Mouginot, B. Scheuchl, M. Van Den Broeke, M. J. Van Wessem, and M. Morlighem, “Four decades of Antarctic Ice Sheet mass balance from 1979–2017,” *Proc. Nat. Acad. Sci.*, vol. 116, no. 4, pp. 1095–1103, 2019.
- [7] M. Donat-Magnin et al., “Future surface mass balance and surface melt in the Amundsen sector of the West Antarctic Ice Sheet,” *Cryosphere*, vol. 15, no. 2, pp. 571–593, 2021.
- [8] R. E. Bell, A. F. Banwell, L. D. Trusel, and J. Kingslake, “Antarctic surface hydrology and impacts on ice-sheet mass balance,” *Nat. Climate Change*, vol. 8, no. 12, pp. 1044–1052, 2018.
- [9] P. K. Munneke, S. R. Ligtenberg, M. R. Van Den Broeke, and D. G. Vaughan, “Firm air depletion as a precursor of Antarctic ice-shelf collapse,” *J. Glaciol.*, vol. 60, no. 220, pp. 205–214, 2014.
- [10] E. Gilbert and C. Kittel, “Surface melt and runoff on Antarctic ice shelves at 1.5°C, 2°C, and 4°C of future warming,” *Geophysical Res. Lett.*, vol. 48, no. 8, 2021, Art. no. e2020GL091733.
- [11] T. Scambos et al., “Ice shelf disintegration by plate bending and hydrofracture: Satellite observations and model results of the 2008 Wilkins ice shelf break-ups,” *Earth Planet. Sci. Lett.*, vol. 280, no. 1–4, pp. 51–60, 2009.
- [12] J. F. Nye, “The distribution of stress and velocity in glaciers and ice-sheets,” *Proc. Roy. Soc. London. Ser. A Math. Phys. Sci.*, vol. 239, no. 1216, pp. 113–133, 1957.
- [13] J. Weertman, “Can a water-filled crevasse reach the bottom surface of a glacier?,” *JASH Pub.*, vol. 95, pp. 139–145, 1973.
- [14] D. R. MacAyeal, O. V. Sergienko, and A. F. Banwell, “A model of viscoelastic ice-shelf flexure,” *J. Glaciology*, vol. 61, no. 228, pp. 635–645, 2015.
- [15] C. J. van der Veen, “Fracture propagation as means of rapidly transferring surface meltwater to the base of glaciers,” *Geophysical Res. Lett.*, vol. 34, no. 1, 2007.
- [16] A. F. Banwell, I. C. Willis, G. J. Macdonald, B. Goodsell, and D. R. MacAyeal, “Direct measurements of ice-shelf flexure caused by surface meltwater ponding and drainage,” *Nat. Commun.*, vol. 10, no. 1, 2019, Art. no. 730.
- [17] R. M. DeConto and D. Pollard, “Contribution of Antarctica to past and future sea-level rise,” *Nature*, vol. 531, no. 7596, pp. 591–597, 2016.
- [18] L. D. Trusel et al., “Divergent trajectories of Antarctic surface melt under two twenty-first-century climate scenarios,” *Nat. Geosci.*, vol. 8, no. 12, pp. 927–932, 2015.

- [19] D. G. Vaughan, "Recent trends in melting conditions on the Antarctic Peninsula and their implications for ice-sheet mass balance and sea level," *Arctic, Antarctic, Alpine Res.*, vol. 38, no. 1, pp. 147–152, 2006.
- [20] P. K. Munneke et al., "Intense winter surface melt on an Antarctic ice shelf," *Geophysical Res. Lett.*, vol. 45, no. 15, pp. 7615–7623, 2018.
- [21] C. L. Jakobs et al., "A benchmark dataset of in situ Antarctic surface melt rates and energy balance," *J. Glaciol.*, vol. 66, no. 256, pp. 291–302, 2020.
- [22] C. Agosta et al., "Estimation of the Antarctic surface mass balance using the regional climate model MAR (1979–2015) and identification of dominant processes," *Cryosphere*, vol. 13, no. 1, pp. 281–296, 2019.
- [23] J. M. Van Wessem et al., "Modelling the climate and surface mass balance of polar ice sheets using RACMO2–Part 2: Antarctica (1979–2016)," *Cryosphere*, vol. 12, no. 4, pp. 1479–1498, 2018.
- [24] L. Zheng, C. Zhou, and Q. Liang, "Variations in Antarctic Peninsula snow liquid water during 1999–2017 revealed by merging radiometer, scatterometer and model estimations," *Remote Sens. Environ.*, vol. 232, 2019, Art. no. 111219.
- [25] J. Lenaerts et al., "Meltwater produced by wind–albedo interaction stored in an East Antarctic ice shelf," *Nat. Climate Change*, vol. 7, no. 1, pp. 58–62, 2017.
- [26] J. Kingslake, J. C. Ely, I. Das, and R. E. Bell, "Widespread movement of meltwater onto and across Antarctic ice shelves," *Nature*, vol. 544, no. 7650, pp. 349–352, 2017.
- [27] Z. Hu, P. K. Munneke, S. Lhermitte, M. Izeboud, and M. Van Den Broeke, "Improving surface melt estimation over the Antarctic Ice sheet using deep learning: A proof of concept over the Larsen Ice Shelf," *Cryosphere*, vol. 15, no. 12, pp. 5639–5658, 2021.
- [28] J. J. Spergel, J. Kingslake, T. Creyts, M. van Wessem, and H. A. Fricker, "Surface meltwater drainage and ponding on Amery Ice Shelf, East Antarctica, 1973–2019," *J. Glaciology*, vol. 67, no. 266, pp. 985–998, 2021.
- [29] M. Dirscherl, A. J. Dietz, C. Kneisel, and C. Kuenzer, "Automated mapping of Antarctic supraglacial lakes using a machine learning approach," *Remote Sens.*, vol. 12, no. 7, 2020, Art. no. 1203.
- [30] R. L. Dell et al., "Supervised classification of slush and ponded water on Antarctic ice shelves using landsat 8 imagery," *J. Glaciology*, vol. 68, no. 268, pp. 401–414, 2022.
- [31] D. K. Hall, R. Williams, K. A. Casey, N. E. DiGirolamo, and Z. Wan, "Satellite-derived, melt-season surface temperature of the Greenland Ice Sheet (2000–2005) and its relationship to mass balance," *Geophysical Res. Lett.*, vol. 33, 2006, Art. no. L11501, doi: [10.1029/2006GL026444](https://doi.org/10.1029/2006GL026444).
- [32] D. K. Hall, J. C. Comiso, N. E. DiGirolamo, C. A. Shuman, J. E. Box, and L. S. Koenig, "Variability in the surface temperature and melt extent of the Greenland Ice Sheet from MODIS," *Geophysical Res. Lett.*, vol. 40, no. 10, pp. 2114–2120, 2013.
- [33] D. K. Hall, R. S. Williams, S. B. Luthcke, and N. E. DiGirolamo, "Greenland Ice Sheet surface temperature, melt and mass loss: 2000–06," *J. Glaciology*, vol. 54, no. 184, pp. 81–93, 2008.
- [34] R. Dell et al., "Lateral meltwater transfer across an Antarctic ice shelf," *Cryosphere*, vol. 14, no. 7, pp. 2313–2330, 2020.
- [35] M. Moussavi, A. Pope, A. R. W. Halberstadt, L. D. Trusel, L. Cioffi, and W. Abdalati, "Antarctic supraglacial lake detection using landsat 8 and Sentinel-2 imagery: Towards continental generation of lake volumes," *Remote Sens.*, vol. 12, no. 1, 2020, Art. no. 134.
- [36] J. F. Arthur, C. R. Stokes, S. S. Jamieson, J. R. Carr, A. A. Leeson, and V. Verjans, "Large interannual variability in supraglacial lakes around East Antarctica," *Nat. Commun.*, vol. 13, no. 1, 2022, Art. no. 1711.
- [37] L. Trusel, K. E. Frey, and S. B. Das, "Antarctic surface melting dynamics: Enhanced perspectives from radar scatterometer data," *J. Geophysical Res.: Earth Surf.*, vol. 117, 2012, Art. no. F02023.
- [38] S. L. Bevan, A. J. Luckman, P. K. Munneke, B. Hubbard, B. Kulesa, and D. W. Ashmore, "Decline in surface melt duration on Larsen C ice shelf revealed by the advanced scatterometer (ASCAT)," *Earth Space Sci.*, vol. 5, no. 10, pp. 578–591, 2018.
- [39] M. Dirscherl, A. J. Dietz, C. Kneisel, and C. Kuenzer, "A novel method for automated supraglacial lake mapping in Antarctica using Sentinel-1 SAR imagery and deep learning," *Remote Sens.*, vol. 13, no. 2, 2021, Art. no. 197.
- [40] D. Liang, H. Guo, L. Zhang, Y. Cheng, Q. Zhu, and X. Liu, "Time-series snowmelt detection over the Antarctic using Sentinel-1 SAR images on Google Earth Engine," *Remote Sens. Environ.*, vol. 256, 2021, Art. no. 112318.
- [41] R. T. Datta et al., "The effect of foehn-induced surface melt on firn evolution over the Northeast Antarctic Peninsula," *Geophysical Res. Lett.*, vol. 46, no. 7, pp. 3822–3831, 2019.
- [42] W. Li, S. Lhermitte, and P. López-Dekker, "The potential of synthetic aperture radar interferometry for assessing meltwater lake dynamics on Antarctic ice shelves," *Cryosphere*, vol. 15, no. 12, pp. 5309–5322, 2021.
- [43] D. Dunmire et al., "Observations of buried lake drainage on the Antarctic Ice sheet," *Geophysical Res. Lett.*, vol. 47, no. 15, 2020, Art. no. e2020GL087970.
- [44] G. Picard and M. Fily, "Surface melting observations in Antarctica by microwave radiometers: Correcting 26-year time series from changes in acquisition hours," *Remote Sens. Environ.*, vol. 104, no. 3, pp. 325–336, 2006.
- [45] M. Tedesco and A. J. Monaghan, "An updated Antarctic melt record through 2009 and its linkages to high-latitude and tropical climate variability," *Geophysical Res. Lett.*, vol. 36, no. 18, 2009.
- [46] M. Tedesco, W. Abdalati, and H. J. Zwally, "Persistent surface snowmelt over Antarctica (1987–2006) from 19.35 GHz brightness temperatures," *Geophysical Res. Lett.*, vol. 34, no. 18, 2007, doi: [10.1029/2007GL031199](https://doi.org/10.1029/2007GL031199).
- [47] O. Torinesi, M. Fily, and C. Genthon, "Variability and trends of the summer melt period of Antarctic ice margins since 1980 from microwave sensors," *J. Climate*, vol. 16, no. 7, pp. 1047–1060, 2003.
- [48] H. Liu, L. Wang, and K. C. Jezek, "Spatiotemporal variations of snowmelt in Antarctica derived from satellite scanning multichannel microwave radiometer and special sensor microwave imager data (1978–2004)," *J. Geophysical Res.: Earth Surf.*, vol. 111, 2006, Art. no. F01003.
- [49] A. Colliander et al., "Ice sheet surface and subsurface melt water discrimination using multi-frequency microwave radiometry," *Geophysical Res. Lett.*, vol. 49, no. 4, 2022, Art. no. e2021GL096599.
- [50] M. Mousavi, A. Colliander, J. Z. Miller, and J. S. Kimball, "A novel approach to map the intensity of surface melting on the Antarctica ice sheet using SMAP L-band microwave radiometry," *IEEE J. Sel. Topics Appl. Earth Observ. Remote Sens.*, vol. 15, pp. 1724–1743, 2022, doi: [10.1109/JSTARS.2022.3147430](https://doi.org/10.1109/JSTARS.2022.3147430).
- [51] M. Leduc-Leballeur, G. Picard, G. Macelloni, A. Mialon, and Y. H. Kerr, "Melt in Antarctica derived from soil moisture and ocean salinity (SMOS) observations at L band," *Cryosphere*, vol. 14, no. 2, pp. 539–548, 2020.
- [52] L. D. Trusel, K. E. Frey, S. B. Das, P. K. Munneke, and M. R. Van Den Broeke, "Satellite-based estimates of Antarctic surface meltwater fluxes," *Geophysical Res. Lett.*, vol. 40, no. 23, pp. 6148–6153, 2013.
- [53] L. Zheng, X. Cheng, X. Shang, Z. Chen, Q. Liang, and K. Wang, "Greenland ice sheet daily surface melt flux observed from space," *Geophysical Res. Lett.*, vol. 49, no. 6, 2022, Art. no. e2021GL096690.
- [54] F. T. Ulaby, R. K. Moore, and A. K. Fung, *Microwave Remote Sensing: Active and Passive*, vol. 3. Boston, MA, USA: Addison-Wesley, 1986.
- [55] S. Colbeck, "Snow-crystal growth with varying surface temperatures and radiation penetration," *J. Glaciology*, vol. 35, no. 119, pp. 23–29, 1989.
- [56] R. E. Brandt and S. G. Warren, "Solar-heating rates and temperature profiles in Antarctic snow and ice," *J. Glaciology*, vol. 39, no. 131, pp. 99–110, 1993.
- [57] D. K. Hall and J. Martinec, "An introduction to the optical, thermal and electrical properties of ice and snow," in *Remote Sensing Ice Snow*. Berlin, Germany: Springer, 1985, pp. 1–9.
- [58] F. Hui et al., "Mapping blue-ice areas in Antarctica using ETM and MODIS data," *Ann. Glaciology*, vol. 55, no. 66, pp. 129–137, 2014.
- [59] M. Tedesco, *Remote Sensing of the Cryosphere*. Hoboken, NJ, USA: Wiley, 2014.
- [60] J. Dozier, S. R. Schneider, and D. F. McGinnis, "Effect of grain size and snowpack water equivalence on visible and near-infrared satellite observations of snow," *Water Resour. Res.*, vol. 17, no. 4, pp. 1213–1221, 1981.
- [61] B. J. Choudhury and A. T. C. Chang, "Two-stream theory of reflectance of snow," *IEEE Trans. Geosci. Electron.*, vol. 17, no. 3, pp. 63–68, Jul. 1979.
- [62] A. Luckman et al., "Surface melt and ponding on Larsen C Ice Shelf and the impact of föhn winds," *Antarctic Sci.*, vol. 26, no. 6, pp. 625–635, 2014.
- [63] I. S. Ashcraft and D. G. Long, "Comparison of methods for melt detection over Greenland using active and passive microwave measurements," *Int. J. Remote Sens.*, vol. 27, no. 12, pp. 2469–2488, 2006.
- [64] J. Shi and J. Dozier, "Inferring snow wetness using C-band data from SIR-C's polarimetric synthetic aperture radar," *IEEE Trans. Geosci. Remote Sens.*, vol. 33, no. 4, pp. 905–914, Jul. 1995.
- [65] D. Hall, R. Williams, J. Barton, O. Sigurdsson, L. Smith, and J. Garvin, "Evaluation of remote-sensing techniques to measure decadal-scale changes of Hofsjökull ice cap, Iceland," *J. Glaciology*, vol. 46, no. 154, pp. 375–388, 2000.

- [66] F. T. Ulaby, R. K. Moore, and A. K. Fung, *Microwave Remote Sensing: Active and Passive* (Microwave Remote Sensing Fundamentals and Radiometry), vol. 1. Norwood, MA, USA: Artech House, 1981.
- [67] T. Nagler, H. Rott, E. Ripper, G. Bippus, and M. Hetzenecker, "Advancements for snowmelt monitoring by means of Sentinel-1 SAR," *Remote Sens.*, vol. 8, no. 4, 2016, Art. no. 348.
- [68] T. L. Mote and M. R. Anderson, "Variations in snowpack melt on the Greenland Ice Sheet based on passive-microwave measurements," *J. Glaciology*, vol. 41, no. 137, pp. 51–60, 1995.
- [69] R. Hofer and C. Mätzler, "Investigations on snow parameters by radiometry in the 3-to 60-mm wavelength region," *J. Geophysical Res.: Oceans*, vol. 85, no. C1, pp. 453–460, 1980.
- [70] M. T. Hallikainen, F. T. Ulaby, and T. E. Van Deventer, "Extinction behavior of dry snow in the 18-to 90-GHz range," *IEEE Trans. Geosci. Remote Sens.*, vol. GE-25, no. 6, pp. 737–745, Nov. 1987.
- [71] A. G. Williamson, A. F. Banwell, I. C. Willis, and N. S. Arnold, "Dual-satellite (Sentinel-2 and landsat 8) remote sensing of supraglacial lakes in Greenland," *Cryosphere*, vol. 12, no. 9, pp. 3045–3065, 2018.
- [72] R. E. Bell et al., "Antarctic ice shelf potentially stabilized by export of meltwater in surface river," *Nature*, vol. 544, no. 7650, pp. 344–348, 2017.
- [73] K. Yang and L. C. Smith, "Supraglacial streams on the Greenland Ice Sheet delineated from combined spectral–shape information in high-resolution satellite imagery," *IEEE Geosci. Remote Sens. Lett.*, vol. 10, no. 4, pp. 801–805, Jul. 2013.
- [74] A. R. W. Halberstadt, C. J. Gleason, M. S. Moussavi, A. Pope, L. D. Trusel, and R. M. DeConto, "Antarctic supraglacial lake identification using Landsat-8 image classification," *Remote Sens.*, vol. 12, no. 8, 2020, Art. no. 1327.
- [75] W. H. Stiles and F. T. Ulaby, "The active and passive microwave response to snow parameters: 1. wetness," *J. Geophysical Res.: Oceans*, vol. 85, no. C2, pp. 1037–1044, 1980.
- [76] A. Johnson, M. Fahnestock, and R. Hock, "Evaluation of passive microwave melt detection methods on Antarctic peninsula ice shelves using time series of Sentinel-1 SAR," *Remote Sens. Environ.*, vol. 250, 2020, Art. no. 112044.
- [77] C. Zhou, L. Zheng, Q. Sun, and R. Liu, "Amery ice shelf surface snowmelt detected by ASCAT and Sentinel-1," *Remote Sens. Lett.*, vol. 10, no. 5, pp. 430–438, 2019.
- [78] R. V. Bothale, P. Rao, C. Dutt, and V. K. Dadhwal, "Detection of snow melt and freezing in Himalaya using OSCAT data," *J. Earth Syst. Sci.*, vol. 124, no. 1, pp. 101–113, 2015.
- [79] H. J. Zwally and S. Fiegles, "Extent and duration of Antarctic surface melting," *J. Glaciology*, vol. 40, no. 136, pp. 463–475, 1994.
- [80] T. L. Mote, M. R. Anderson, K. C. Kuivinen, and C. M. Rowe, "Passive microwave-derived spatial and temporal variations of summer melt on the Greenland Ice Sheet," *Ann. Glaciology*, vol. 17, pp. 233–238, 1993.
- [81] J. M. Ramage and B. L. Isacks, "Determination of melt-onset and refreeze timing on Southeast Alaskan icefields using SSM/I diurnal amplitude variations," *Ann. Glaciology*, vol. 34, pp. 391–398, 2002.
- [82] M. Tedesco, M. Brodzik, R. Armstrong, M. Savoie, and J. Ramage, "Pan Arctic terrestrial snowmelt trends (1979–2008) from spaceborne passive microwave data and correlation with the Arctic Oscillation," *Geophysical Res. Lett.*, vol. 36, 2009, Art. no. L21402, doi: [10.1029/2009GL039672](https://doi.org/10.1029/2009GL039672).
- [83] L. Zheng, C. Zhou, T. Zhang, Q. Liang, and K. Wang, "Recent changes in pan-Antarctic region surface snowmelt detected by AMSR-E and AMSR2," *Cryosphere*, vol. 14, no. 11, pp. 3811–3827, 2020.
- [84] L. Zheng, C. Zhou, R. Liu, and Q. Sun, "Antarctic snowmelt detected by diurnal variations of AMSR-E brightness temperature," *Remote Sens.*, vol. 10, no. 9, 2018, Art. no. 1391.
- [85] K. A. Semmens, J. Ramage, A. Bartsch, and G. E. Liston, "Early snowmelt events: Detection, distribution, and significance in a major sub-Arctic watershed," *Environ. Res. Lett.*, vol. 8, no. 1, 2013, Art. no. 014020.
- [86] W. Abdalati and K. Steffen, "Passive microwave-derived snow melt regions on the Greenland Ice Sheet," *Geophysical Res. Lett.*, vol. 22, no. 7, pp. 787–790, 1995, doi: [10.1029/95GL00433](https://doi.org/10.1029/95GL00433).
- [87] N. Gorelick, M. Hancher, M. Dixon, S. Ilyushchenko, D. Thau, and R. Moore, "Google Earth Engine: Planetary-scale geospatial analysis for everyone," *Remote Sens. Environ.*, vol. 202, pp. 18–27, 2017.
- [88] D. G. Long, P. J. Hardin, and P. T. Whiting, "Resolution enhancement of spaceborne scatterometer data," *IEEE Trans. Geosci. Remote Sens.*, vol. 31, no. 3, pp. 700–715, May 1993.
- [89] J. Arigony-Neto et al., "Spatial and temporal changes in dry-snow line altitude on the Antarctic Peninsula," *Climatic Change*, vol. 94, no. 1, pp. 19–33, 2009.
- [90] L. Zheng and C. Zhou, "Comparisons of snowmelt detected by microwave sensors on the Shackleton ice shelf, East Antarctica," *Int. J. Remote Sens.*, vol. 41, no. 4, pp. 1338–1348, 2020.
- [91] G. Koh and R. Jordan, "Sub-surface melting in a seasonal snow cover," *J. Glaciology*, vol. 41, no. 139, pp. 474–482, 1995.
- [92] L. Liang, H. Guo, X. Li, and X. Cheng, "Automated ice-sheet snowmelt detection using microwave radiometer measurements," *Polar Res.*, vol. 32, no. 1, 2013, Art. no. 19746.
- [93] N. Steiner and M. Tedesco, "A wavelet melt detection algorithm applied to enhanced resolution scatterometer data over Antarctica (2000–2009)," *Cryosphere*, vol. 8, pp. 25–40, 2014.
- [94] G. E. Liston and J.-G. Winther, "Antarctic surface and subsurface snow and ice melt fluxes," *J. Climate*, vol. 18, no. 10, pp. 1469–1481, 2005.
- [95] K. A. Kilpatrick, G. P. Podestá, and R. Evans, "Overview of the NOAA/NASA advanced very high resolution radiometer pathfinder algorithm for sea surface temperature and associated matchup database," vol. 106, no. C5, pp. 9179–9197, May 2001.
- [96] M. Brodzik, D. Long, M. Hardman, A. Paget, and R. Armstrong, "MEaSURES calibrated enhanced-resolution passive microwave daily EASE-grid 2.0 brightness temperature ESDR, version 1, various resolutions, cylindrical equal area projection, boulder," Colorado USA, NASA National Snow and Ice Data Center Distributed Active Archive Center, 2016. Accessed: May 1, 2022. [Online]. Available: <https://doi.org/10.5067/MEASURES/CRYOSPHERE/NSIDC-0630.001>
- [97] J. Mougintot, B. Scheuchl, and E. Rignot, "MEaSURES Antarctic boundaries for IPY 2007-2009 from satellite radar, version 2, national snow and ice data center," 2017. Accessed: May 1, 2022. [Online]. Available: <https://doi.org/10.5067/AXE4121732AD>
- [98] L. Gerrish, P. Fretwell, and P. Cooper, "High resolution vector polylines of the Antarctic coastline (7.4), U.K. polar data centre, natural environment research council, U.K. research & innovatio," 2021, accessed: Apr. 20, 2022. [Online] Available: <https://doi.org/10.5285/bc71347d-298a-4df3-88b0-cb9a908db166>
- [99] T. Slater et al., "A new digital elevation model of Antarctica derived from CryoSat-2 altimetry," *Cryosphere*, vol. 12, no. 4, pp. 1551–1562, 2018.
- [100] A. F. Banwell et al., "32-year record-high surface melt in 2019/2020 on north George VI Ice Shelf, Antarctic Peninsula," *Cryosphere*, vol. 15, pp. 909–925, 2020.
- [101] J. F. Arthur, C. R. Stokes, S. S. Jamieson, J. R. Carr, and A. A. Leeson, "Distribution and seasonal evolution of supraglacial lakes on Shackleton Ice Shelf, East Antarctica," *Cryosphere*, vol. 14, no. 11, pp. 4103–4120, 2020.
- [102] H.-R. Hannula and J. Pulliainen, "Spectral reflectance behavior of different boreal snow types," *J. Glaciology*, vol. 65, no. 254, pp. 926–939, 2019.
- [103] R. Bintanja and M. R. van den Broeke, "The influence of clouds on the radiation budget of ice and snow surfaces in Antarctica and Greenland in summer," *Int. J. Climatol.: J. Roy. Meteorological Soc.*, vol. 16, no. 11, pp. 1281–1296, 1996.
- [104] M. Van Den Broeke, C. Reijmer, D. Van As, and W. Boot, "Daily cycle of the surface energy balance in Antarctica and the influence of clouds," *Int. J. Climatol.: J. Roy. Meteorological Soc.*, vol. 26, no. 12, pp. 1587–1605, 2006.
- [105] K. Van Tricht et al., "Clouds enhance Greenland Ice Sheet meltwater runoff," *Nat. Commun.*, vol. 7, no. 1, 2016, Art. no. 10266.
- [106] M. Izeboud, S. Lhermitte, K. Van Tricht, J. Lenaerts, N. Van Lipzig, and N. Wever, "The spatiotemporal variability of cloud radiative effects on the Greenland Ice Sheet surface mass balance," *Geophysical Res. Lett.*, vol. 47, no. 12, 2020, Art. no. e2020GL087315.
- [107] M. King, S. Platnick, W. P. Menzel, S. A. Ackerman, and A. H. Paul, "Spatial and temporal distribution of tropospheric clouds observed by MODIS on-board the terra and aqua satellites," *IEEE Trans. Geosci. Remote Sens.*, vol. 51, no. 7, pp. 3826–3852, Jul. 2013.
- [108] G. Picard, M. Sandells, and H. Löwe, "SMRT: An active-passive microwave radiative transfer model for snow with multiple microstructure and scattering formulations (v1.0)," *Geoscientific Model Develop.*, vol. 11, no. 7, pp. 2763–2788, 2018.
- [109] G. Picard, M. Leduc-Leballeur, A. F. Banwell, L. Brucker, and G. Macelloni, "The sensitivity of satellite microwave observations to liquid water in the Antarctic snowpack," *The Cryosphere*, vol. 16, pp. 5061–5083, 2022. [Online]. Available: <https://doi.org/10.5194/tc-16-5061-2022>
- [110] C. Vargel et al., "Arctic and subarctic snow microstructure analysis for microwave brightness temperature simulations," *Remote Sens. Environ.*, vol. 242, 2020, Art. no. 111754.
- [111] C. Mätzler, "Improved born approximation for scattering of radiation in a granular medium," *J. Appl. Phys.*, vol. 83, no. 11, pp. 6111–6117, 1998.

- [112] J.-G. Winther, M. N. Jaspersen, and G. E. Liston, "Blue-ice areas in Antarctica derived from NOAA AVHRR satellite data," *J. Glaciology*, vol. 47, no. 157, pp. 325–334, 2001.
- [113] L. Montgomery et al., "Hydrologic properties of a highly permeable firn aquifer in the Wilkins Ice Shelf, Antarctica," *Geophysical Res. Lett.*, vol. 47, no. 22, 2020, Art. no. e2020GL089552.
- [114] A. Wager, "Flooding of the ice shelf in George VI sound," *Brit. Antarctic Surv. Bull.*, vol. 28, pp. 71–74, 1972.
- [115] J. M. Reynolds, "Lakes on George VI ice shelf, Antarctica," *Polar Rec.*, vol. 20, no. 128, pp. 425–432, 1981.
- [116] J. V. Turton, A. Kirchgassner, A. N. Ross, J. C. King, and P. K. Munneke, "The influence of föhn winds on annual and seasonal surface melt on the Larsen C ice shelf, Antarctica," *Cryosphere*, vol. 14, no. 11, pp. 4165–4180, 2020.
- [117] Q. Libois et al., "Influence of grain shape on light penetration in snow," *Cryosphere*, vol. 7, no. 6, pp. 1803–1818, 2013.
- [118] H.-R. Hannula, K. Heinilä, K. Böttcher, O.-P. Mattila, M. Salminen, and J. Pulliainen, "Laboratory, field, mast-borne and airborne spectral reflectance measurements of boreal landscape during spring," *Earth Syst. Sci. Data*, vol. 12, no. 1, pp. 719–740, 2020.
- [119] Z. Hu, P. K. Munneke, S. Lhermitte, M. Dirscherl, C. Ji, and M. van den Broeke, "FABIAN: A daily product of fractional Austral-summer blue ice over Antarctica during 2000–2021 based on MODIS imagery using Google Earth Engine," *Remote Sens. Environ.*, vol. 280, 2022, Art. no. 113202.



Sophie de Roda Husman received the B.Sc. and M.Sc. degrees in civil engineering from the Delft University of Technology, Delft, the Netherlands, in 2017 and 2020, respectively. She is currently working toward the Ph.D. degree at the Delft University of Technology from January 2021.

Her research focuses on Antarctic surface melt and hydrology using multisource satellite imagery.



Zhongyang Hu received the Ph.D. degree in remote sensing from University of Wuerzburg, Germany, in 2020.

He is currently a Postdoc Researcher with the Institute for Marine and Atmospheric Research Utrecht, Utrecht University, Utrecht, the Netherlands. His research interests include time-series analysis based on long-term satellite imagery and modeling land surface dynamics using machine learning and deep learning techniques.



Bert Wouters received the M.Sc. and Ph.D. degrees in aerospace engineering from the Delft University of Technology, Delft, the Netherlands, in 2004 and 2010, respectively.

He was a Postdoc with Koninklijk Nederlands Meteorologisch Instituut, De Bilt, the Netherlands, the Universities of Boulder, USA, and Bristol, U.K., and the IMAU institute, Utrecht University. Since 2018, he has been with the Faculty of Civil Engineering and Geosciences, Delft University of Technology, Delft, the Netherlands. His research focuses on remote sensing of the climate, in particular, of the cryosphere, and combining these observations with model data.

remote sensing of the climate, in particular, of the cryosphere, and combining these observations with model data.



Peter Kuipers Munneke is currently a researcher with the Institute for Marine and Atmospheric Research, Utrecht University, Utrecht, the Netherlands. He specializes in ice sheet mass balance, polar meteorology, and firn. He has been working with climate models, automatic weather station observations, and firn models. He is actively involved in science outreach and popular-scientific communication about weather, climate, and the polar regions.



Sanne Veldhuijsen received the B.Sc. degree in 2018, in earth sciences and the M.Sc. degree in 2020, in hydrology from Utrecht University, Utrecht, the Netherlands, where she is currently working toward the Ph.D. degree with the Institute for Marine and Atmospheric Research Utrecht (IMAU), working on improved modeling of the current and future Antarctic firn layer for which she uses the IMAU Firn Densification model (IMAU-FDM) in combination with *in situ* and remote sensing measurements.



Stef Lhermitte received the Ph.D. degree in bioscience engineering from KU Leuven, Leuven, Belgium, in 2008.

He is currently a Remote Sensing Scientist with specific interest in the use of multisource remote sensing and land surface modeling to assess cryosphere, atmosphere, and ecosystem dynamics. He was on several international Postdocs positions (with CEAZA, KNMI, and KU Leuven), where he worked on broad range of remote sensing technologies in a variety of applications ranging from cryospheric and atmospheric sciences to ecology and hydrology. Since 2022, he has been an Associate Research Professor with KU Leuven, which he combined with a position as an Associate Professor with the Delft University of Technology, Delft, the Netherlands, since 2016. His research focuses on the development of innovative remote sensing methods for assessing land-atmosphere interactions in order to assess the effect of climate (change) on the cryosphere, ecosystem dynamics, the hydrological cycle, sea level rise, etc., and their feedbacks on (future) climate.